

Electric field tunable superconductivity with competing orders in near magic-angle twisted bilayer graphene

Ranit Dutta^{1*}, Ayan Ghosh^{1†}, Shinjan Mandal¹, K. Watanabe², T. Taniguchi³, H.R. Krishnamurthy¹, Sumilan Banerjee¹, Manish Jain¹ and Anindya Das^{1‡}

¹*Department of Physics, Indian Institute of Science, Bangalore, 560012, India.*

²*Research Center for Functional Materials, National Institute for Materials Science, Tsukuba, Japan.*

³*International Center for Material Nanoarchitectonics, National Institute for Materials Science, Tsukuba, Japan*

Superconductivity (SC) in twisted bilayer graphene (tBLG) has been explored by varying carrier concentrations, twist angles, and screening strength, with the aim of uncovering its origin and possible connections to strong electronic correlations in narrow bands and various resulting broken symmetries. However, the link between the tBLG band structure and the onset of SC and other orders largely remains unclear. In this study, we address this crucial gap by examining in-situ band structure tuning of a near magic-angle ($\theta \approx 0.95^\circ$) tBLG device with displacement field (D) and reveal remarkable competition between SC and other broken symmetries. At zero D , the device exhibits superconducting signatures without the resistance peak at half-filling, a characteristic signature with a strong electronic correlation. As D increases, the SC is suppressed, accompanied by the appearance of a resistance peak at half-filling. Hall density measurements reveal that at zero D , SC arises around the van Hove singularity (vHs) from an isospin or spin-valley unpolarized band. At higher D , the suppression of SC coincides with broken isospin symmetry near half-filling with lifted degeneracy ($g_d \sim 2$). Additionally, when SC is suppressed at higher D , density waves around the superconducting dome are seen. These findings, with our theoretical calculations, highlight the competition between SC and other orders, and the stabilization of the latter by the electric field enhanced nesting in the band structure of tBLG.

Introduction:

A relative twist angle between two or more van der Waals layers¹⁻¹¹, leading to the formation of moiré superlattice, has opened up a completely new field of condensed matter research known as ‘twistronics’. Observations of interaction-driven emergent phenomena like superconductivity (SC)^{1,2,6,8-21}, correlated Mott insulators^{2,3}, orbital ferromagnetism²², anomalous Hall²³ and quantized anomalous Hall effect²⁴, ne-

*equally contributed

†equally contributed

‡anindya@iisc.ac.in

maticity¹³, chern insulators^{25,26}, strange metal²⁷, giant thermopower¹⁴ and breakdown of semi-classical description of Mott's formula^{14,28} are ubiquitous in this area. Among the family of twisted heterostructures, magic-angle twisted bilayer graphene (MAtBLG)^{1-3,12,13,17,19,25-27,29-32} with a twist angle of $\theta_M \simeq 1.1^\circ$ between two sheets of graphene monolayer is being extensively studied for hosting flat bands³³ and having a rich phase diagram with such strongly correlated phases. Inter-layer hybridization between the rotated layers facilitates the formation of these isolated flat bands which causes the effective electronic kinetic energy to become much smaller than the effective coulomb interactions³ leading to the realization of such correlated phases. The appearance of correlated insulators (CI)^{2,3} at integer moiré filling ν and a superconducting dome when the CIs are doped away from the integer filling^{1,2} shows a strong resemblance to the behavior of high- T_c (> 100 K) cuprate superconductors³⁴.

Recent studies have, however, raised questions as to whether and to what extent superconductivity in tBLG is intimately connected with correlation effects¹⁶⁻¹⁸. In these reports, superconductivity has been observed even in the absence of correlated insulator states by varying the dielectric thickness to control the coulomb screening¹⁷, and even at angles detuned away from θ_M , with the SC phase sometimes taking over the whole of the phase space without any signature of correlated states¹⁶⁻¹⁸. The decoupling of superconductivity and correlated insulator behavior in the presence of screened coulomb interactions¹⁹ or the increased bandwidth of the flat bands (angles away from $\theta_M \pm 0.05^\circ$) indicate that these two phenomena may not be always intimately connected, and may even be competing^{17,18} and electron-phonon mechanism may be playing a significant role in the origin of superconductivity in tBLG^{17,35-37}. Thus, unlike other graphene-based systems such as Bernal bilayer graphene (BBG)^{38,39}, rhombohedral trilayer graphene (RTG)⁴⁰, ABC-trilayer graphene/aligned with hBN⁴¹, alternately twisted trilayer^{8,9}, and multi-layer graphene^{10,11}, where superconductivity consistently emerges close to other symmetry-broken phases, it remains unclear whether superconductivity and other symmetry-broken phases are fundamentally linked in twisted bilayer graphene (tBLG).

To answer these questions, one needs to investigate specific features of tBLG, other than electron-electron and electron-phonon interaction, e.g., band structure details such as van Hove singularity (vHs) that can crucially influence superconductivity. However, the exploration of how the appearance of superconductivity is connected to the features of such band structure details in tBLG is missing in the literature. Here, we address this issue through the remarkable in-situ tuning of the band structure by a displacement field that continuously tunes a vHs further away from half-filling and thus induces other symmetry-breaking orders, presumably competing with SC. As shown schematically in Fig. 1, applying a perpendicular electric field can tune the band structure of a tBLG with a twist angle slightly away from the magic angle, and can give insights into the intimate connection between the band structure and SC. Thus, we present a comprehensive study on tuning the SC phase of a near-magic angle tBLG ($\sim 0.95^\circ$) device as a function of a perpendicular electric field (displacement field, D). At zero displacement field ($D = 0.00$ V/nm), the device shows resistance peaks at the Dirac point (CNP) and full band filling ($\nu = \pm 4$) also known as superlattice gaps, but

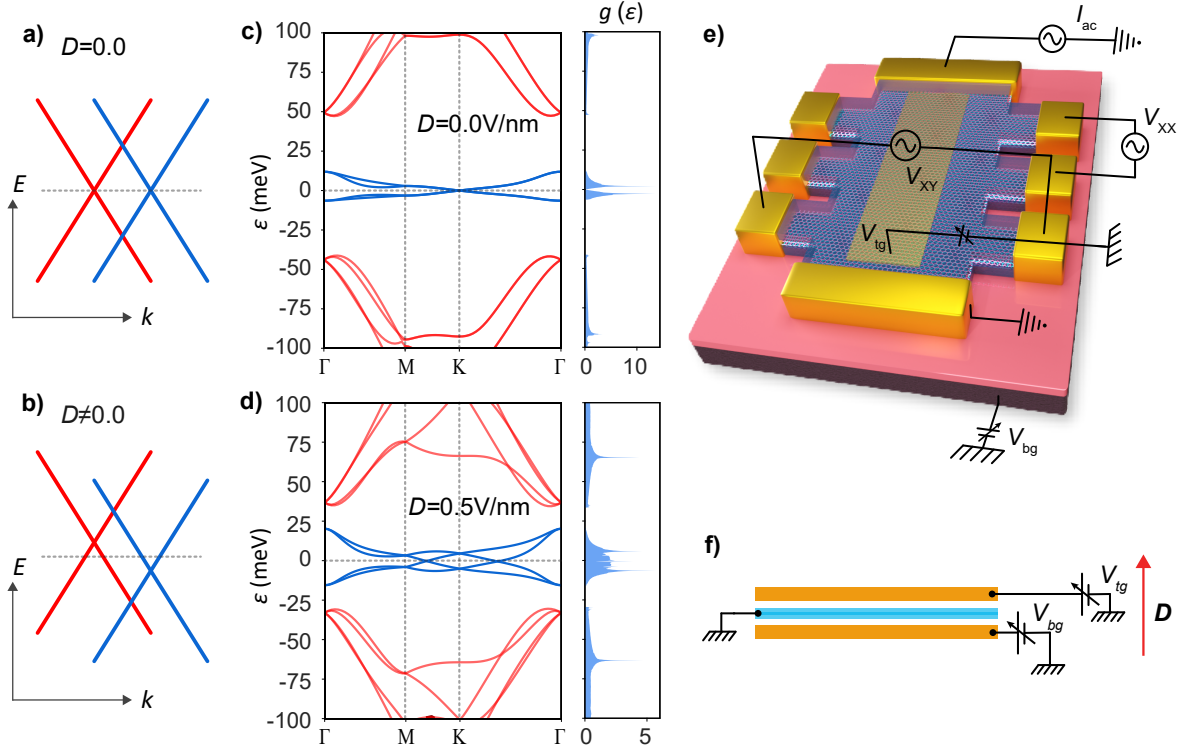


Figure 1: **Band structure and device schematic.** Schematic presentation of band crossing of top and bottom layer graphene at zero D , **a)** and finite D , **b)**. The calculated band structures using a tight-binding model on relaxed structures of twist angle $\sim 0.95^\circ$ tBLG for $D = 0$, **c)** and $D = 0.5\text{V/nm}$, **d)**. **e)** Device set-up for measuring R_{xx} and R_{xy} . Using the combination of a metal top gate (V_{tg}) and a global SiO₂/Si back gate (V_{bg}), the carrier density, n , and the perpendicular displacement field, D , were controlled independently. **f)** The schematic for the positive displacement field when V_{bg} is positive but V_{tg} is negative. All the measurements are done with constant current bias and using standard low-frequency lock-in technique at frequency $f = 13\text{ Hz}$ in a cryo-free dilution refrigerator.

without any signature of resistance peaks at half-filling ($\nu \sim \pm 2$). Most interestingly, the device shows the signature of SC with resistance dropping to almost zero with decreasing temperature away from half-filling ($\nu \sim +2.7$). Typical behaviors such as a superconducting dome with temperature (T), non-linear current-voltage ($I - V$) characteristics, and suppression of the superconducting phase with a magnetic field (B) establish the robustness of the SC phase of the device at $D = 0.00$ V/nm. With increasing D , the SC phase is suppressed with the appearance of the resistance peak at the half-filling ($\nu \sim 2$). The tuning of the SC is further quantified from the D dependent critical temperature, T_c , critical D.C. bias current, I_c , and critical magnetic field, B_c , (both parallel and perpendicular). To understand the role of the band structure, we study the Hall density (Hall filling/Normalized Hall density, ν_H) as a function of the filling (ν) at different D , which reveals the following: (i) at $D = 0.00$ V/nm, the SC arises precisely around the van Hove singularity (vHs) from an isospin-unpolarized band with degeneracy, $g_d = 4$, (ii) at higher D magnitudes, the suppression of SC is concomitant with the broken isospin symmetry near half-filling, with lifted degeneracy of $g_d \sim 2$. Further, when the SC is suppressed at finite D , the signature of density waves around the SC dome is seen as periodic resistance oscillations. These observations, along with our theoretical calculations, clearly demonstrate the presence of competing orders in tBLG with different orders stabilized at different electric fields due to the enhanced nesting in the band structure.

Device set-up and characterization: For our study, we have fabricated a dual-gated hBN encapsulated twisted bilayer graphene device using the modified ‘cut and stack’ technique from an exfoliated single monolayer graphene sheet on a SiO_2/Si substrate⁴². Details of fabrication are mentioned in the supplementary information SI-1. A metal layer above the top hBN acts as the top gate of the device, whereas the Silicon (Si) layer acts as the global back gate. The dual-gated device structure helps to tune the number density, n , and the perpendicular displacement field, D , independently⁴⁻⁹ in our tBLG device, as shown schematically in Fig. 1f (see SI-2 for details). Fig. 1e shows the device schematic together with the measurement scheme to measure longitudinal (R_{xx}) and transverse (R_{xy}) resistance in a standard Hall-bar geometry set-up. Fig. 2a shows the longitudinal resistance, R_{xx} , versus the filling factor, ν , with increasing temperature from the base temperature of $T = 20$ mK up to 25 K at $D = 0.00$ V/nm. The carrier density, n , measured relative to the charge neutrality point (CNP) is converted to moiré filling factor, $\nu = \frac{4n}{n_s}$, where n_s is the requisite carrier density to fill/empty the low energy flat bands (i.e 4 electron/holes per moiré superlattice unit cell)^{1,2}. High insulating resistance peaks at moiré integer filling, $\nu = \pm 4$, on either side of the CNP indicates the presence of a single-particle band gap above and below the low energy flat bands. The twist angle from the carrier densities for $\nu = \pm 4$ corresponds to $\theta \approx 0.95^\circ \pm 0.02^\circ$ for our device, which is around 13% smaller than the magic angle $\theta_M \approx 1.1^\circ$. Note that the twist angle variation across the several contacts remains less than 3% in our device, as shown in SI-Fig.1c,d. Unlike other tBLG devices closer to the magic-angle^{1-3,12,17,18}, we do not observe any resistance peaks corresponding to the correlated insulators at half-filling, $\nu = \pm 2$, or at other integer fillings². All the measurements are done using the standard lock-in technique at $f \sim 13$ Hz in a cryo-free dilution fridge for several thermal cycles.

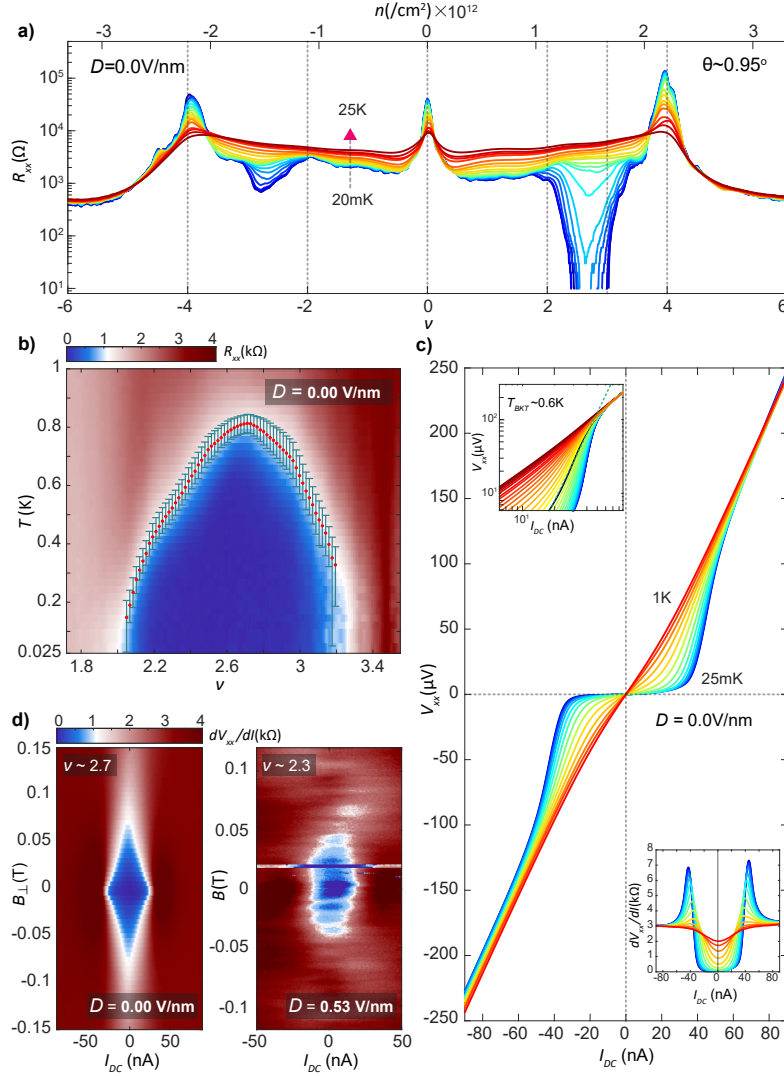


Figure 2: **Robust superconductivity at zero D .** **a)** Measured R_{xx} versus carrier filling, ν , from $T = 20$ mK up to 25 K at $D = 0$ V/nm. The resistance peaks at the Dirac point, and full band filling ($\nu = +4, -4$) are seen without any signature of resistance peaks at other integer fillings. The R_{xx} value approaches close to zero on the electron side at $T = 20$ mK between $\nu \sim 2 - 3$ marking the superconducting region. **b)** 2-d colormap of R_{xx} as a function of ν and T showing the superconductivity dome around optimal doping, $\nu_c \sim 2.6 - 2.7$. The red dots are the critical temperatures, T_c , corresponding to the 50% value of normal state resistance, R_n . The error bars refer to the corresponding temperatures, T , at which R_{xx} drops to 60% and 40% of R_n . **c)** $I - V$ characteristics of SC region at $\nu \approx 2.7$ with variation of T from 25 mK to 1 K. The lower inset shows the dV_{xx}/dI versus I_{DC} . In the upper inset, $V_{xx} \propto I^3$ behavior is clearly seen suggesting a typical 2D superconductor with a Berezinskii-Kosterlitz-Thouless transition at $T_{BKT} \sim 600$ mK. **d)** dV_{xx}/dI versus I_{DC} and B_{\perp} for $\nu, D = 2.7, 0.00$ V/nm (left panel) and $2.3, 0.50$ V/nm (right panel). The Fraunhofer-like oscillations can be seen when the SC is suppressed at higher D .

Superconductivity at zero D : As seen in Fig. 2a, we see a clear signature of superconductivity on the electron side with the R_{xx} value going down to almost zero between $\nu = 2.2$ and $\nu = 3$ at the base temperature of $T = 20$ mK. Though the signature of resistance decrement with lowering of the temperature on the hole side between $\nu = -2.2$ and $\nu = -3$ can be seen in Fig. 2a, in this region the R_{xx} value remains finite at the lowest measured temperature (20 mK). From here on, we will only focus on the superconducting region on the electron side ($2 < \nu < 3$). Fig. 2b shows $R_{xx}(\nu, T)$ in the 2-d colormap. A superconducting dome around $\nu_c \sim 2.6 - 2.7$ (optimal doping) is clearly visible. The temperature dependence of V_{xx} versus I_{DC} traces are shown in Fig. 2c, which are obtained by integrating dV_{xx}/dI as a function of I_{DC} as shown in the lower inset of Fig. 2c. The traces in Fig. 2c show the classic evolution of 2D superconductors from step-like transitions at low temperature to ohmic dependence around 1 K. The upper inset in Fig. 2c shows the BKT (Berezinskii-Kosterlitz-Thouless) transition, where the evolution of the $V_{xx} \sim I_{DC}^\alpha$ power law near the critical bias current gives the BKT transition temperature, $T_{BKT} \sim 0.6K$ corresponding to $V_{xx} \sim I_{DC}^3$. Fig. 2b and 2c establish the robustness of the superconductivity in our device at $D = 0.00$ V/nm. Further, the superconductivity is killed by applying a perpendicular magnetic field ($B_{c\perp} \sim 60 - 70$ mT) as shown in Fig. 2d left panel. Though the Fraunhofer-like oscillation pattern ^{1,2,6,8,12,14,16} is not seen at $D = 0.00$ V/nm, it is visible when the superconductivity gets suppressed at finite D , as shown in the right panel of Fig. 2d (details in SI-4).

Tuning superconductivity with D : In this section, we discuss our main results on tuning the SC with D . Fig. 3a shows the variation of R_{xx} with ν at the base temperature for several D . The corresponding 2-d colormap of R_{xx} with ν and D is shown in SI-Fig. 2a. As shown in Fig. 3a, with increasing positive D , the resistance peak values at the CNP and full band filling ($\nu = \pm 4$) slightly decrease while the most dramatic effect with D can be seen on the electron-doped side, particularly between $\nu \sim 1 - 3$. The superconducting region's width around $\nu \sim 2.7$ gradually shrinks as the D value crosses ~ 0.20 V/nm. As SC weakens with D , a resistance peak emerges at $\nu \sim 2$ together with an increase in the background resistance value around $\nu \sim 1$. This could be an indication of the onset of correlation physics, which is discussed in the next section while presenting the Hall density measurements. The concomitance between the SC suppression and resistance peak appearance with increasing D suggests that the two phases compete rather than being intimately connected. Note that the strength of SC also decreases with negative D , but the effect remains weaker compared to the positive D as discussed in SI-3 (see SI-Fig. 2b). The superconducting region being tuned by D has already been reported in other systems like alternately twisted magic-angle trilayer graphene, ^{8,9} quadra layer and pentalayer ^{10,11} graphene, but not so far seen in tBLG. Ref ¹² on MATBLG reports an appearance of a resistive peak at half filling on the hole side ($\nu = -2$) with increasing D , but there are no indications of the modification of the strength of the superconducting phase with D . The tunability of the SC phase in our near magic-angle tBLG can be further seen in the superconducting dome, as shown in Fig. 3b and 3c. It can be seen that compared to Fig. 2b at $D = 0.00$ V/nm, at $D = 0.60$ V/nm in Fig. 3c, both the width (in ν) of the SC region and T_c are reduced significantly. Fig. 3d shows R_{xx} versus T at the optimal doping ($\nu \sim 2.7$) for several D , emphasizing the tunability of SC with D . In Fig. 4, we have

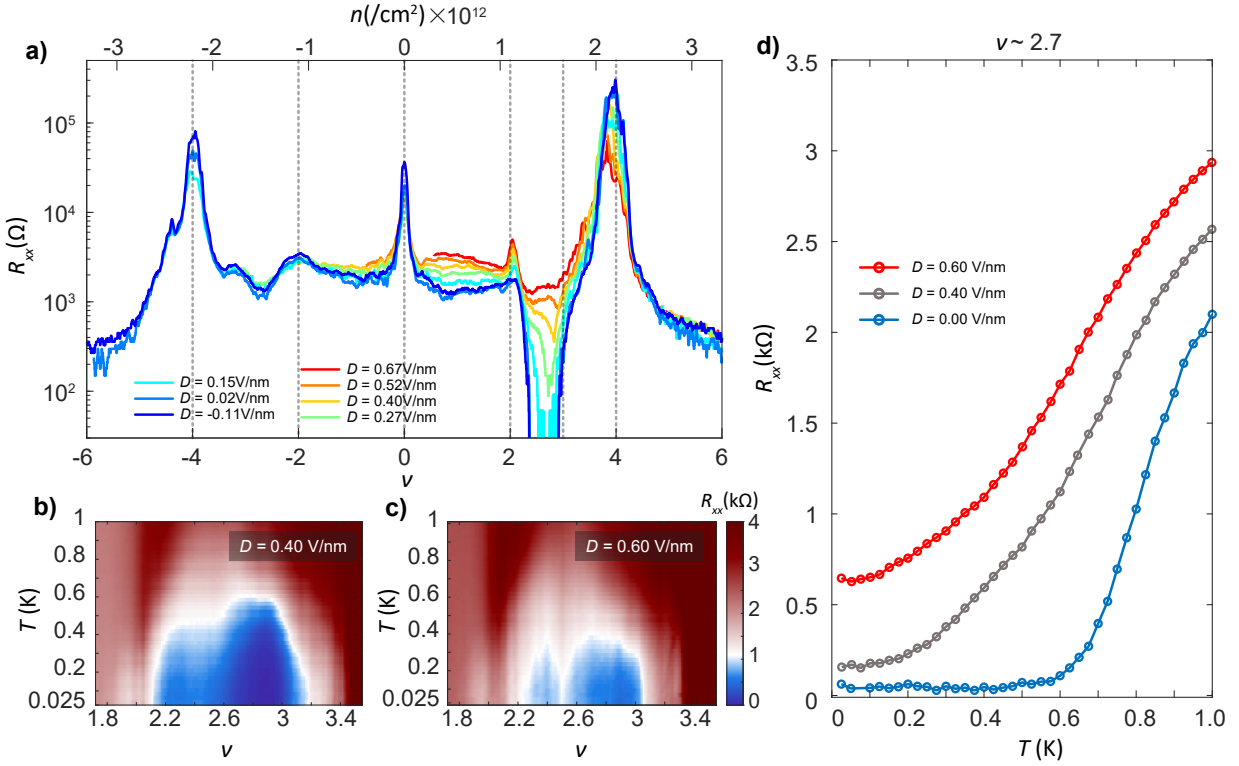


Figure 3: **Tunability of superconductivity with D .** **a)** R_{xx} versus ν at the base temperature for different D . The SC weakens with increasing D , and a resistance peak emerges at $\nu \sim 2$ with a background resistance increment around $\nu \sim 1$. **b)** and **c)** represent the superconducting domes of $R_{xx}(\nu, T)$ for $D = 0.40$ V/nm and 0.60 V/nm, respectively. The width and height of the superconducting domes show a decrement with increasing D compared to the zero D case in Fig. 2b. **d)** Plots of R_{xx} vs T for different D fields at $\nu \sim 2.7$.

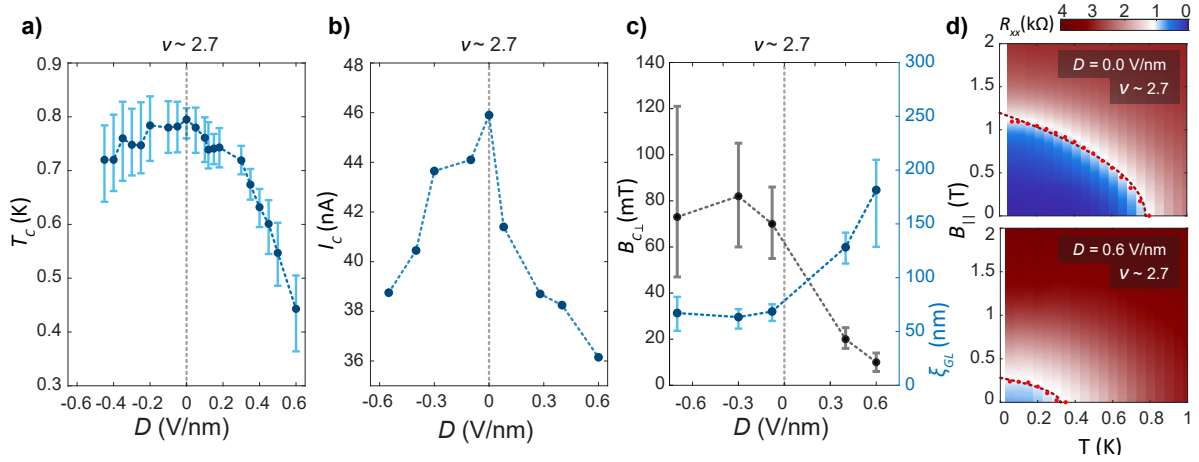


Figure 4: **Superconductivity metrics with D .** **a)** Variation of T_c with D at $\nu \sim 2.7$. The values of T_c were approximated as the temperatures at which R_{xx} drops to 50% of normal state resistance, R_n , for the respective D fields. The error bars represent the temperatures corresponding to 60% and 40% of R_n . **b)** Variation of I_c with D at $\nu \sim 2.7$. **c)** Variation of $B_{c\perp}$ (left axis) and corresponding Ginzburg-Landau coherence length, ξ_{GL} (right axis), with D at $\nu \sim 2.7$. The error bars for $B_{c\perp}$ represent the required magnetic field, B_{\perp} , to cross 60% and 40% thresholds of R_n . **d)** R_{xx} versus B_{\parallel} and T for zero D (top panel) and 0.60 V/nm (bottom panel). The temperature dependence of $B_{c\parallel}$ (red dots) is fitted (dashed black line) to extract the critical parallel magnetic field at zero temperature, $B_{c\parallel}^0 \sim 1.2$ T and 0.3 T for $D = 0.00$ V/nm and 0.60 V/nm, respectively, which matches well with the Pauli limit calculated from $B_p = 1.76k_B T_c^0 \sqrt{2}/g\mu_B$, where T_c^0 is the zero magnetic field critical temperature, g is Landé g-factor, and μ_B is Bohr magneton.

summarized the tunability of several SC metrics with D . The variation of T_c , I_c , and perpendicular $B_{c\perp}$ with D are shown in Figs. 4a, 4b, 4c, respectively. Raw data related to these plots are shown in SI-5 and SI-6 (SI-Fig. 4-9); which also describes the method (R_{xx} value to one-half of its normal state value^{2,6,8}) used to extract T_c , I_c , and $B_{c\perp}$. The right side y-axis of Fig. 4c shows the variation of the superconducting coherence length (ξ_{GL}) with D . At a given D , the Ginzburg Landau coherence length is extracted from the inferred zero temperature limit of the critical magnetic field, $B_{c\perp}^0$ (see SI-6 (IV) for details). Fig. 4d shows the effect on the SC phase of a parallel magnetic field, B_{\parallel} , and T at $D = 0.00$ V/nm (top panel) and $D = 0.60$ V/nm (bottom panel). The temperature dependence of $B_{c\parallel}$ (red dots in Fig. 4d) is fitted to the phenomenological relation: $T/T_c^0 = 1 - (B_{c\parallel}/B_{c\parallel}^0)^2$, where T_c^0 is the superconducting critical temperature at zero B , and the fitting gives the critical parallel magnetic field in the zero temperature limit, $B_{c\parallel}^0$, which matches well with the Pauli limit^{6,8,29} (see SI-6 (V) for details) at $D = 0.00$ and 0.60 V/nm. Note that the asymmetry in SC metrics with positive and negative D seen in our experiment in Fig. 4 could be related to the asymmetry in the dielectric environment of the top and bottom layer graphene (different thicknesses of the top and bottom hBN, metallic top gate versus SiO₂/Si back gate, and discussed in detail in SI-2 and SI-3), and has been reported for alternately twisted trilayer graphene^{8,9}.

Hall density and isospin symmetry breaking with D : So far, we have discussed how the SC is tuned with D ; however, to see its connection with the characteristics of the band structure, in this section, we present the Fermiology measurements like the Hall density (n_H). The single particle low-energy band of tBLG has four flavors, corresponding to two valleys and two spins, as schematically shown in Fig. 5a. Fig. 5d shows the variation of the measured Hall filling, ν_H ($\equiv 4n_H/n_s$) (see SI-7 (II) for details), with the moiré filling factor, ν , at $D = 0.00$ V/nm on the electron-doped side at $B_{\perp} = 0.5$ T (anti-symmetrized by measuring at $B_{\perp} = \pm 0.5$ T, see SI-7 for details). At $B_{\perp} = 0.5$ T, the SC is killed, and it can be seen from Fig. 5b that ν_H increases with a linear slope until $\nu \sim 2$, and beyond that, ν_H increases rapidly and diverges (with value $> \pm 200$, see SI-Fig. 10a) on either side of $\nu \sim 2.7$, where it changes sign. This is a clear signature of (the Fermi level crossing) a vHs⁹. It can be seen from the R_{xx} versus ν plot in Fig. 5b ($B_{\perp} = 0$ T) that the SC phase arises around the vHs, and the linear slope in the Hall filling (versus filling) measurement confirms that all the four flavors are equally populated with the charge carriers as shown schematically in Fig. 5g, implying that the SC arises from an isospin-unpolarized band. A similar result for twisted double bilayer graphene stabilized by WSe₂⁶ has recently been reported, where the superconductivity emerges from unpolarized states near the van Hove singularities. Figs 5c,e show similar plots for $D = 0.50$ V/nm, in which case, initially, the ν_H increases with slope one; however, before reaching the vHs at $\nu \sim 3.0$, there is a suppression of ν_H around $\nu \sim 2$, where a resistance peak (R_{xx}) concomitantly emerges as shown in Fig. 5c, with no SC. The 2-d colormap of ν_H with ν and D is shown in SI-Fig. 11a. To understand the suppression in Hall filling with ν , in Fig. 5f we plot $\nu_H - \nu$ versus ν , which remains close to zero at $D = 0.00$ V/nm, reconfirming the degeneracy of $g_d = 4$ of the occupied bands. As can be seen from the figure, with increasing D the values of $\nu_H - \nu$ deviate from zero and become negative between $\nu \sim 2$ and vHs, and their values head towards ~ -2 , attaining the value of ~ -1.6 at $D \sim 0.70$ V/nm, which indicates

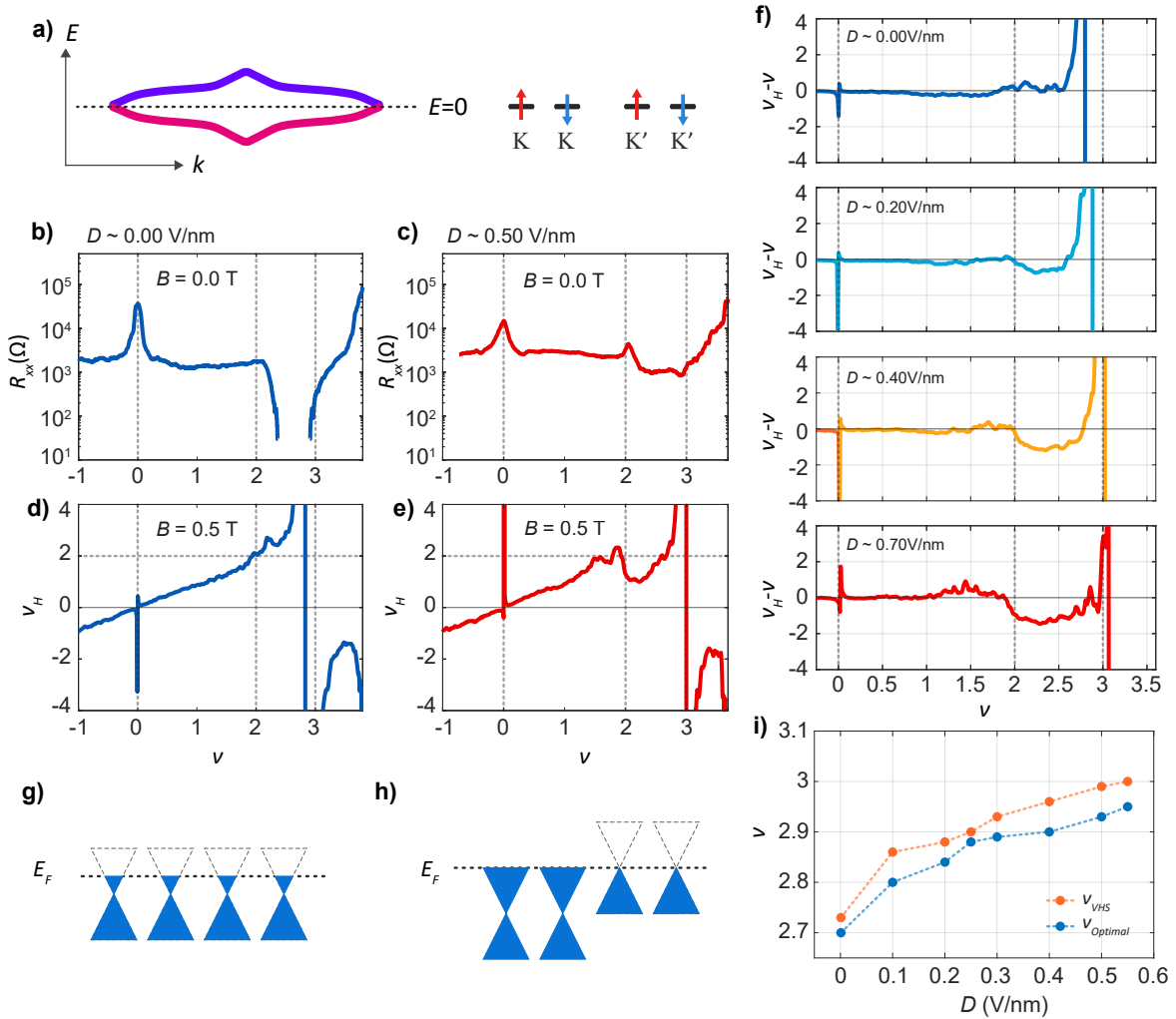


Figure 5: **Hall density and isospin symmetry breaking with D .** **a)** Schematic representation of isospin unpolarized single particle low energy degenerate bands in tBLG. **b), c)** Longitudinal resistance, R_{xx} vs the filling factor, ν , for displacement field, $D = 0.00$ V/nm and 0.50 V/nm respectively. **d), e)** Normalized Hall density ν_H vs ν for the same D values as in **(b), (c)**. **f)** $\nu_H - \nu$ vs ν plots for several D . **g)** Schematic representation of unpolarized isospin flavors at zero D when all the Dirac-like bands are equally populated with degeneracy $g_d = 4$. **h)** Schematic representation for polarized isospin flavors with degeneracy $g_d = 2$. **i)** Filling factors of the optimal doping point of the superconducting phase, $\nu_{optimal}$ and the van Hove singularity (vHs) position, ν_{vHs} with D . Both $\nu_{optimal}$ and ν_{vHs} track each other and increase with increasing D .

broken isospin symmetry with $g_d \sim 2$ as schematically shown in Fig. 5h. The signatures of broken isospin symmetry are also seen in the Landau Fan diagram shown in SI-Fig. 12.

Competing orders and discussion: To summarize the above section, for our device, SC arises around the vHs from an unpolarized band but becomes weaker with broken isospin symmetry (or cascaded transition/Dirac revival) at $\nu \sim 2$, which is responsible for the appearance of the peak in R_{xx} . These two competing phases, SC and the phase with isospin polarization are stabilized respectively for small and large values of the displacement field. Though with increasing D the SC phase gets suppressed, the intimate connection between the diverging density of states (vHs) and SC can be seen in Fig. 5i, where the filling values corresponding to the vHs (ν_{vHs}) and optimal doping for the SC ($\nu_{optimal}$) are plotted versus D and show a close correspondence. In our theory, we capture the shift of the vHs with increasing D as shown in SI-Fig. 20. Although the calculated fillings corresponding to the vHs do not precisely match experimental observations, the theory captures the essential features qualitatively. We would like to mention here that there are several other systems, such as rhombohedral trilayer graphene⁴⁰, alternately twisted trilayer^{8,9} and multilayer graphene^{10,11}, in which the SC phase emerges directly from a phase where only two out of the four isospin components are occupied. In comparison, in twisted bilayer graphene, there have been contrasting results between MATBLG, and detuned¹⁸ or screened tBLG^{17,19}. In this work, in a tBLG slightly away from the magic angle, we have shown that upon tuning with D , the two phases seem to compete rather than being intimately connected. Further, in Fig. 6 we show the appearance of other competing orders like density waves arising from spontaneously broken translational symmetry of the moiré lattice when the SC is suppressed at higher D ⁴³. Fig. 6a show how the R_{xx} changes with perpendicular magnetic field, B_{\perp} , and ν at $D = 0.00$ V/nm (left panel) and 0.40 V/nm (right panel). Nearly periodic oscillations ($\Delta\nu \sim 1/10$) in R_{xx} become prominent at higher D once the SC gets weakened with B_{\perp} , which can be seen clearly in Fig. 6a (right panel), and as cut plots in Fig. 6b. The details are discussed in SI-13. These periodic oscillations around the vHs are most likely the manifestation of translation symmetry breaking due to a charge density wave instability and have been reported in the literature⁴³. Fermi contours around the vHs in our theoretically calculated band structure offer some insights as to how this comes about. Fig. 6c displays the Fermi contours as computed from a tight binding model (see SI-14 for details). One can see that for higher D the contours look approximately like flattened ellipses, with nearly parallel sections signifying nested Fermi contours, (rightmost panel), near the M points of the Brillouin Zone. However, such nesting is absent at smaller D fields. This indicates the possibility of the formation of charge density waves driven by nesting in the band-structure at finite D . In SI-14, we have summarized our theoretical results obtained for various values of fillings, ν and D . Similar tendencies for CDW formation have been predicted previously in MATBLG⁴⁴.

In summary, our findings emphasize the influence of band structure tuning through an external electric field on the emergence of superconductivity and other orders in near magic-angle twisted bilayer graphene. Our results highlight the close connection between the divergent density of states in the electronic structures and the presence of superconductivity. Furthermore, we observe that superconductivity diminishes with

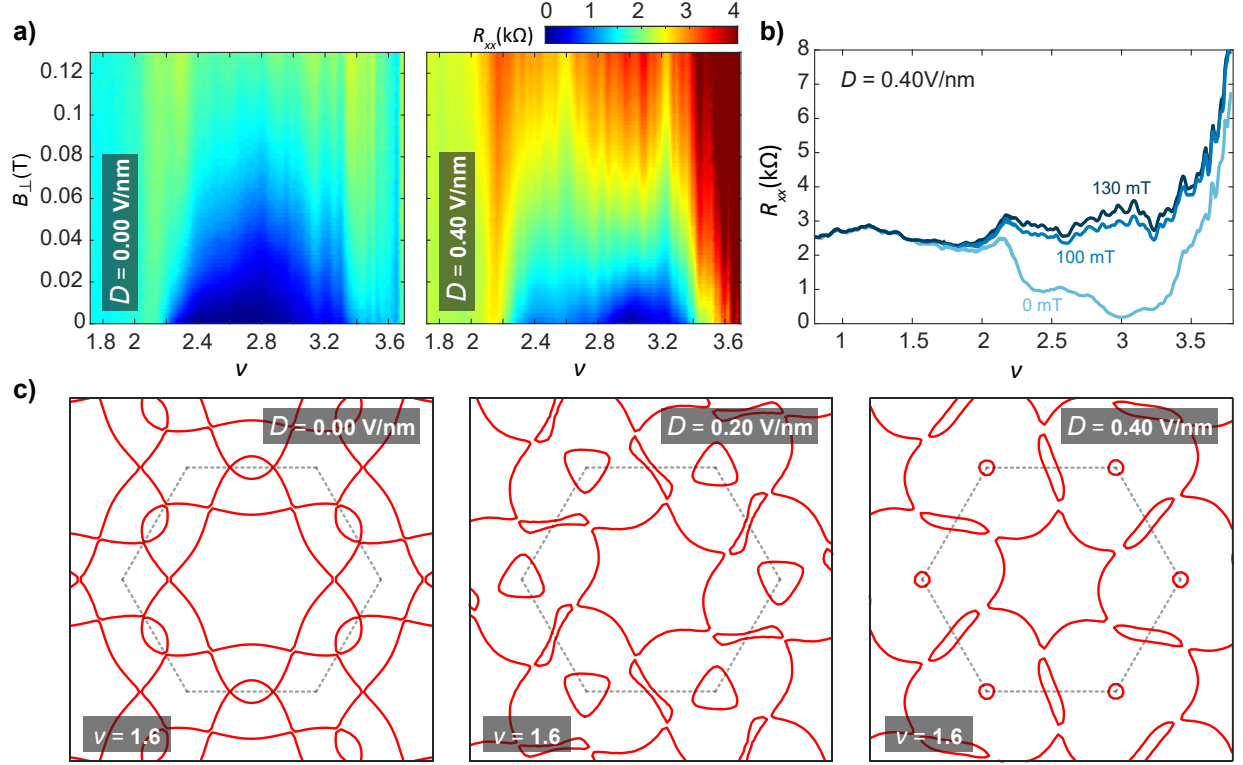


Figure 6: **Density wave instability around the SC phase.** **a)** R_{xx} as a function of ν and B_{\perp} demonstrating the superconductivity dome for $D = 0.00$ V/nm (left) and 0.40 V/nm (right) measured at $T \sim 25$ mK. Prominent oscillations in R_{xx} as a function of ν are seen with increasing B_{\perp} for $D = 0.40$ V/nm after superconductivity is suppressed. **b)** Cut lines for $B_{\perp} = 0$ T, 100 mT and 130 mT at $D = 0.40$ V/nm. The oscillations in R_{xx} with ν ($2.2 < \nu < 3.3$) reveals a period of $\Delta\nu \sim 1/10$. **c)** Fermi contour plots at a filling of $\nu = 1.6$ are computed using the tight-binding model. At $D = 0.00$ V/nm the Fermi contours do not show any nesting. But at higher D the formation of flattened elliptical Fermi contours near the M points of the Brillouin Zone indicates nesting. The magnitudes of these nesting vectors are $\sim |\vec{K}|/10$ indicating that they could result in CDW phases leading to the R_{xx} oscillations (SI-13,14 for details).

alterations to the electronic structure when isospin polarization and density waves are stabilized. Our results are consistent with the recent theoretical study showing the suppression of SC with electric field in tBLG, and highlight how the origin of SC in tBLG is special compared to other twisted and untwisted graphene-based heterostructures⁴⁵. We believe that our study carries broad implications for advancing our understanding of superconductivity as well as other phases in graphitic van der Waals heterostructures, and paves the way for further explorations in the future.

Acknowledgements

A.D. thanks Prof. Ashvin Vishwanath, Prof. Mohit Randeria, and Prof. Nandini Trivedi for the useful discussions. R.D. is grateful to Manabendra Kuiri, Arup Kumar Paul, Ravi Kumar, Saurabh Kumar Srivastav, Souvik Chakraborty, and Ujjal Roy for numerous discussions on the fabrication of twisted heterostructures. R.D. and A.G. thank Ujjal Roy, Saurabh Kumar Srivastav, Ravi Kumar, and Souvik Chakraborty for their assistance while doing measurements in the He³ cryo-stat and cryo-free dilution refrigerator (Oxford Triton and Oxford Proteox). H.R.K. and M.J. gratefully acknowledge the National Supercomputing Mission of the Department of Science and Technology, India, and the Science and Engineering Research Board of the Department of Science and Technology, India, for financial support under Grants No. DST/NSM/R&D HPC Applications/2021/23 and No. SB/DF/005/2017, respectively. H.R.K. also acknowledges support from the Indian National Science Academy under its grant no. INSA/SP/SS/2023/. A.D. thanks the Department of Science and Technology (DST) and Science and Engineering Research Board (SERB), India, for financial support (SP/SERB-22-0387) and acknowledges the Swarnajayanti Fellowship of the DST/SJF/PSA-03/2018-19. A.D. also thanks CEFIPRA project SP/IFCP-22-0005. Growing the hBN crystals received support from the Japan Society for the Promotion of Science (KAKENHI grant nos. 19H05790, 20H00354 and 21H05233) to K.W. and T.T.

Author contributions

R.D. contributed to device fabrication. R.D. and A.G. contributed to data acquisition and analysis. A.G. also contributed to developing measuring codes. S.M., H.R.K., S.B., and M.J. contributed to the development of the theory. K.W. and T.T. synthesized the hBN single crystals. A.D. contributed to conceiving the idea and designing the experiment, data interpretation, and analysis. All the authors contributed to the data interpretation and writing the manuscript.

Competing financial interests

The authors declare no competing interests.

Methods

Device fabrication and measurement scheme: The devices consist of hBN-encapsulated twisted bilayer graphene (tBLG) on a SiO₂/Si substrate. The typical length and width of the devices are 6 μm and 2 μm , respectively. The usual ‘tear and stack’ technique^{1,3} with a modification is used to fabricate the device and is described in detail in the supplementary information (SI-1). We carried out low-temperature transport measurements at 20 \sim 25 mK in a cryo-free dilution refrigerator. Using a constant bias current of $I \leq 5$ nA, the four-probe longitudinal (V_{xx}) and transverse voltage (V_{xy}) were measured using a lock-in amplifier at a low frequency (~ 13 Hz).

Theory: A tBLG structure of twist angle $\theta = 0.95^\circ$ was generated using the TWISTER code⁴⁶. The atomic positions were then relaxed in LAMMPS⁴⁷ up to a force tolerance of 10^{-6} eV/Å. Classical force fields were used to model the interatomic interactions, with Tersoff⁴⁸ as the intra-layer potential and DRIP⁴⁹ as the inter-layer potential. The electronic band structures were computed using a tight binding model with the transfer integrals approximated using the Slater-Koster formalism⁵⁰. The displacement fields were integrated into the calculations as on-site terms within each layer, enabling the assessment of their impact on the electronic properties of the system. Although the doping levels, at which the van Hove singularities (vHs) occurred in our calculations are lower than those observed experimentally, the qualitative behavior and the evolution of the vHs on the electron side with displacement field are consistent with the experimental findings. Further details are available in the Supplementary Information (SI-14).

Data availability: All the relevant non-analytical line-plot data generated or measured during this study are included in this published article (and its supplementary information files). Additional information related to this work is available from the corresponding author upon reasonable request.

References

1. Cao, Y. *et al.* Unconventional superconductivity in magic-angle graphene superlattices. *Nature* **556**, 43–50 (2018).
2. Lu, X. *et al.* Superconductors, orbital magnets and correlated states in magic-angle bilayer graphene. *Nature* **574**, 653–657 (2019).
3. Cao, Y. *et al.* Correlated insulator behaviour at half-filling in magic-angle graphene superlattices. *Nature* **556**, 80–84 (2018).
4. Liu, X. *et al.* Tunable spin-polarized correlated states in twisted double bilayer graphene. *Nature* **583**, 221–225 (2020).

5. Cao, Y. *et al.* Tunable correlated states and spin-polarized phases in twisted bilayer–bilayer graphene. *Nature* **583**, 215–220 (2020).
6. Su, R., Kouri, M., Watanabe, K., Taniguchi, T. & Folk, J. Superconductivity in twisted double bilayer graphene stabilized by wse2. *Nature Materials* **22**, 1332–1337 (2023).
7. Kouri, M. *et al.* Spontaneous time-reversal symmetry breaking in twisted double bilayer graphene. *Nature Communications* **13**, 6468 (2022).
8. Park, J. M., Cao, Y., Watanabe, K., Taniguchi, T. & Jarillo-Herrero, P. Tunable strongly coupled superconductivity in magic-angle twisted trilayer graphene. *Nature* **590**, 249–255 (2021).
9. Hao, Z. *et al.* Electric field–tunable superconductivity in alternating-twist magic-angle trilayer graphene. *Science* **371**, 1133–1138 (2021).
10. Park, J. M. *et al.* Robust superconductivity in magic-angle multilayer graphene family. *Nature Materials* **21**, 877–883 (2022).
11. Zhang, Y. *et al.* Promotion of superconductivity in magic-angle graphene multilayers. *Science* **377**, 1538–1543 (2022).
12. Yankowitz, M. *et al.* Tuning superconductivity in twisted bilayer graphene. *Science* **363**, 1059–1064 (2019).
13. Cao, Y. *et al.* Nematicity and competing orders in superconducting magic-angle graphene. *Science* **372**, 264–271 (2021).
14. Paul, A. K. *et al.* Interaction-driven giant thermopower in magic-angle twisted bilayer graphene. *Nature Physics* 1–8 (2022).
15. Codecido, E. *et al.* Correlated insulating and superconducting states in twisted bilayer graphene below the magic angle. *Science Advances* **5**, eaaw9770 (2019).
16. Arora, H. S. *et al.* Superconductivity in metallic twisted bilayer graphene stabilized by wse2. *Nature* **583**, 379–384 (2020).
17. Stepanov, P. *et al.* Untying the insulating and superconducting orders in magic-angle graphene. *Nature* **583**, 375–378 (2020).
18. Saito, Y., Ge, J., Watanabe, K., Taniguchi, T. & Young, A. F. Independent superconductors and correlated insulators in twisted bilayer graphene. *Nature Physics* **16**, 926–930 (2020).
19. Liu, X. *et al.* Tuning electron correlation in magic-angle twisted bilayer graphene using coulomb screening. *Science* **371**, 1261–1265 (2021).

20. Tian, H. *et al.* Evidence for dirac flat band superconductivity enabled by quantum geometry. *Nature* **614**, 440–444 (2023).
21. Po, H. C., Zou, L., Vishwanath, A. & Senthil, T. Origin of mott insulating behavior and superconductivity in twisted bilayer graphene. *Phys. Rev. X* **8**, 031089 (2018).
22. Sharpe, A. L. *et al.* Emergent ferromagnetism near three-quarters filling in twisted bilayer graphene. *Science* **365**, 605–608 (2019).
23. Tseng, C.-C. *et al.* Anomalous hall effect at half filling in twisted bilayer graphene. *Nature Physics* **18**, 1038–1042 (2022).
24. Serlin, M. *et al.* Intrinsic quantized anomalous hall effect in a moiré heterostructure. *Science* **367**, 900–903 (2020).
25. Wu, S., Zhang, Z., Watanabe, K., Taniguchi, T. & Andrei, E. Y. Chern insulators, van Hove singularities and topological flat bands in magic-angle twisted bilayer graphene. *Nature Materials* **20**, 488–494 (2021).
26. Das, I. *et al.* Symmetry-broken chern insulators and rashba-like landau-level crossings in magic-angle bilayer graphene. *Nature Physics* **17**, 710–714 (2021).
27. Cao, Y. *et al.* Strange metal in magic-angle graphene with near planckian dissipation. *Physical review letters* **124**, 076801 (2020).
28. Ghawri, B. *et al.* Breakdown of semiclassical description of thermoelectricity in near-magic angle twisted bilayer graphene. *Nature Communications* **13**, 1522 (2022).
29. Cao, Y., Park, J. M., Watanabe, K., Taniguchi, T. & Jarillo-Herrero, P. Pauli-limit violation and re-entrant superconductivity in moiré graphene. *Nature* **595**, 526–531 (2021).
30. Lin, J.-X. *et al.* Spin-orbit-driven ferromagnetism at half moiré filling in magic-angle twisted bilayer graphene. *Science* **375**, 437–441 (2022).
31. Zondiner, U. *et al.* Cascade of phase transitions and dirac revivals in magic-angle graphene. *Nature* **582**, 203–208 (2020).
32. Wong, D. *et al.* Cascade of electronic transitions in magic-angle twisted bilayer graphene. *Nature* **582**, 198–202 (2020).
33. Bistritzer, R. & MacDonald, A. H. Moiré bands in twisted double-layer graphene. *Proceedings of the National Academy of Sciences* **108**, 12233–12237 (2011).
34. Xu, Z. A., Ong, N. P., Wang, Y., Kakeshita, T. & Uchida, S. Vortex-like excitations and the onset of superconducting phase fluctuation in underdoped La_{2-x}Sr_xCuO₄. *Nature* **406**, 486–488 (2000).

35. Lian, B., Wang, Z. & Bernevig, B. A. Twisted bilayer graphene: A phonon-driven superconductor. *Physical review letters* **122**, 257002 (2019).
36. Cea, T. & Guinea, F. Coulomb interaction, phonons, and superconductivity in twisted bilayer graphene. *Proceedings of the National Academy of Sciences* **118**, e2107874118 (2021).
37. Shavit, G., Berg, E., Stern, A. & Oreg, Y. Theory of correlated insulators and superconductivity in twisted bilayer graphene. *Physical review letters* **127**, 247703 (2021).
38. Zhou, H. *et al.* Isospin magnetism and spin-polarized superconductivity in bernal bilayer graphene. *Science* **375**, 774–778 (2022).
39. Zhang, Y. *et al.* Enhanced superconductivity in spin–orbit proximitized bilayer graphene. *Nature* **613**, 268–273 (2023).
40. Zhou, H., Xie, T., Taniguchi, T., Watanabe, K. & Young, A. F. Superconductivity in rhombohedral trilayer graphene. *Nature* **598**, 434–438 (2021).
41. Chen, G. *et al.* Signatures of tunable superconductivity in a trilayer graphene moiré superlattice. *Nature* **572**, 215–219 (2019).
42. Ghosh, A. *et al.* Evidence of compensated semimetal with electronic correlations at charge neutrality of twisted double bilayer graphene. *Communications Physics* **6**, 360 (2023).
43. Lin, J.-X. *et al.* Zero-field superconducting diode effect in small-twist-angle trilayer graphene. *Nature Physics* **18**, 1221–1227 (2022).
44. Isobe, H., Yuan, N. F. Q. & Fu, L. Unconventional superconductivity and density waves in twisted bilayer graphene. *Phys. Rev. X* **8**, 041041 (2018).
45. Long, M., Pozo, A. J., Cruz, H. S., Pantaleon, P. A. & Guinea, F. Evolution of superconductivity in twisted graphene multilayers. *Private communication* .
46. Naik, S., Naik, M. H., Maity, I. & Jain, M. Twister: Construction and structural relaxation of commensurate moiré superlattices. *Computer Physics Communications* **271**, 108184 (2022).
47. Thompson, A. P. *et al.* LAMMPS—a flexible simulation tool for particle-based materials modeling at the atomic, meso, and continuum scales. *Computer Physics Communications* **271**, 108171 (2022).
48. Kınacı, A., Haskins, J. B., Sevik, C. & Çağın, T. Thermal conductivity of BN-C nanostructures. *Physical Review B* **86**, 115410 (2012).
49. Wen, M., Carr, S., Fang, S., Kaxiras, E. & Tadmor, E. B. Dihedral-angle-corrected registry-dependent interlayer potential for multilayer graphene structures. *Physical Review B* **98**, 235404 (2018).

50. Moon, P. & Koshino, M. Energy spectrum and quantum Hall effect in twisted bilayer graphene. *Physical Review B* **85**, 195458 (2012).

Supplementary Information: Electric field tunable superconductivity with competing orders in near magic-angle twisted bilayer graphene

Ranit Dutta^{1*}, Ayan Ghosh^{1†}, Shinjan Mandal¹, K. Watanabe², T. Taniguchi³, H.R. Krishnamurthy¹,
Sumilan Banerjee¹, Manish Jain¹ and Anindya Das^{1‡}

¹*Department of Physics, Indian Institute of Science, Bangalore, 560012, India.*

²*Research Center for Functional Materials, National Institute for Materials Science, Tsukuba, Japan.*

³*International Center for Material Nanoarchitectonics, National Institute for Materials Science, Tsukuba, Japan*

*equally contributed

†equally contributed

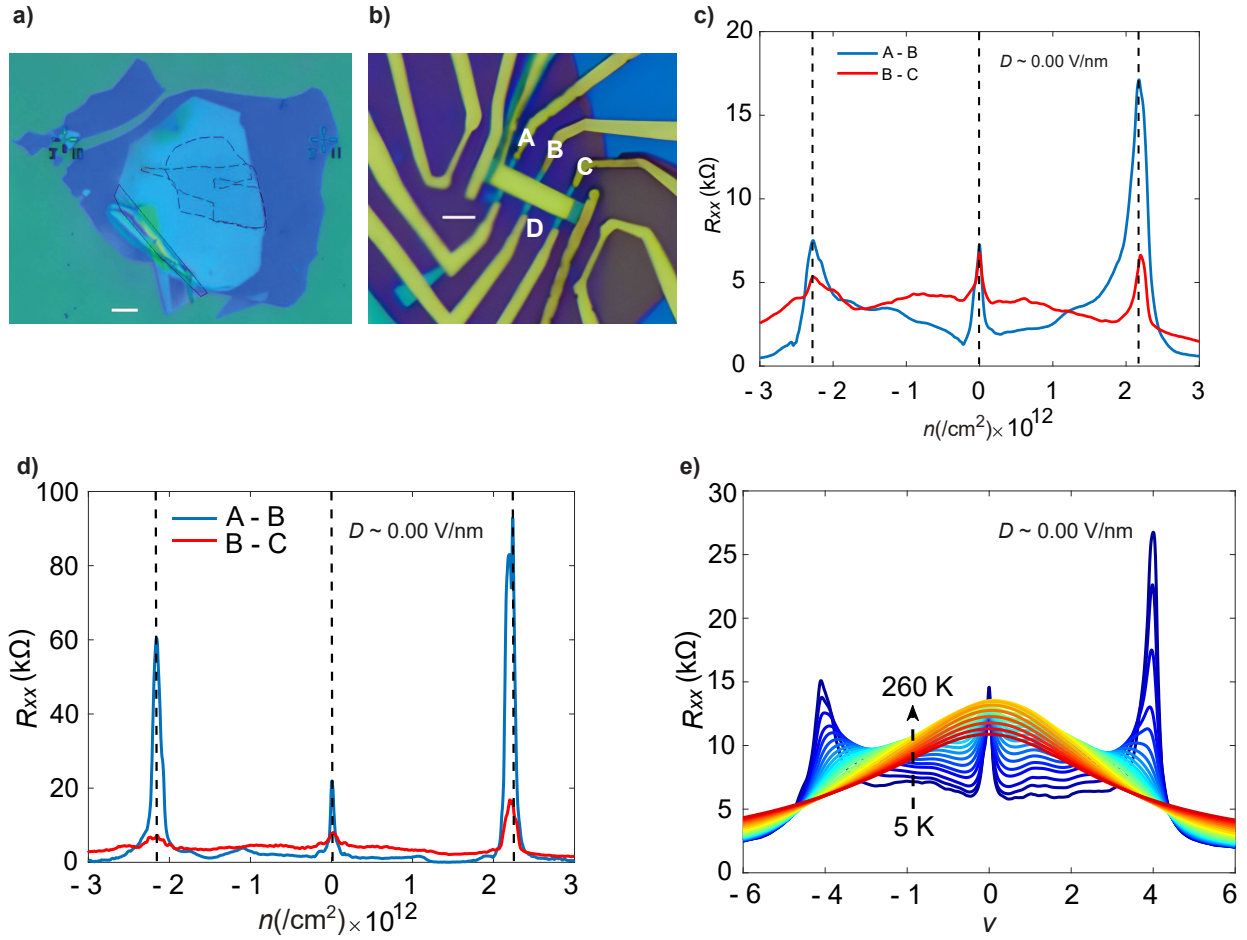
‡anindya@iisc.ac.in

SI-1: Device fabrication, device optical image, device response, and twist angle determination

We have used the well-established "tear and stack" [1, 2, 3, 4, 5, 6, 7] method, with some modifications, to fabricate our twisted bilayer graphene (tBLG) device. First, we exfoliate hBN (thickness $\sim 25 - 30$ nm), while graphene flakes are exfoliated on separate SiO₂/ Si substrates. We then use the optical microscope to identify the required flakes for hBN encapsulation and the graphene flakes for making a twisted bilayer. After identification, we pick up an hBN flake using a transparent PDMS-polypropyl carbonate (PPC) stamp. We use a hemispherically shaped PDMS on one end of a glass slide and cover it with a PPC film to make the PDMS-PPC stamp [8, 9]. This PDMS-PPC-hBN stamp is then used to pick up the 'pre-cut' graphene layers sequentially to form the twisted bilayers. The two graphene layers come from a single larger monolayer graphene flake which we pre-cut using a sharp optical fiber tip under an optical microscope [9, 10], unlike in the "tear and stack" method. The pre-cutting eliminates the strain and folding in the graphene flakes arising due to the tearing process. To introduce the twist angle between the graphene layers, we first pick up one part of the 'pre-cut' graphene with the PDMS-PPC-hBN stamp at $T \sim 40^{\circ}$ C, then rotate the substrate containing the other half of the graphene flake by $\theta = 1.0^{\circ}$ using a rotation stage (with a precision of $\theta = 0.04^{\circ}$) by maintaining the same pick-up temperature as the first graphene flake. Finally, we pick up another hBN flake at $T \sim 60^{\circ}$ C to encapsulate the tBLG layers. The entire stack is then released from the PDMS-PPC stamp on a freshly cleaved SiO₂/ Si substrate (dimension ~ 1 cm²) at $\sim 80^{\circ}$ C. The substrate is further cleaned in acetone for a few hours to remove the PPC residue deposited while transferring the heterostructure to the substrate. The optical image of the twisted heterostructure can be seen in SI-Fig. 1a.

To make the electrical contacts (1-D edge contacts [11]), the substrate is spin-coated (at 3000 rpm) with two layers of negative e-beam resist - one layer of 495A4 and on top of it another layer of 950A4. However, instead of the usual temperature of 180° C, each PMMA layer is baked at 120° C for 15 minutes. This low-temperature baking is done to avoid thermal relaxation of the twist angle between the two graphene layers. Then the contacts are defined using standard e-beam lithography (EBL). After developing the exposed area of the e-beam resist, the contacts are etched with CHF₃-O₂ (gas flow rate ratio $\sim 10 : 1$) plasma [12] followed by thermal deposition (base pressure $\sim 1e - 7$ mbar) of Cr/ Pd/ Au (5 nm/ 10 nm/ 70 nm). For the dual-gated structure, after fabricating the 1-D edge contacts we define the area of the top gate by EBL after another round of spin-coating with resists, and after developing a metallic top gate layer is formed by depositing Cr/ Au (5 nm/ 70 nm) in the defined region on top of the top hBN. We make our device in the shape of standard Hall-bar geometry. We define the shape by EBL and after developing the PMMA exposed by the e-beam, we perform RIE-F (dry etch: fluorine chemistry) to remove the parts of the heterostructure to define the Hall-bar geometry. The optical image of the final device can be seen in SI-Fig. 1b.

Near Magic angle tBLG: The twist-angle θ of the tBLG device is determined from the carrier number densities at the full band filling peaks with respect to the CNP in R_{xx} . The area of the superlattice unit cell for a twist angle θ is given by $A \sim \sqrt{3}a^2/2\theta^2$ [1, 2, 3, 4, 5, 6, 7, 9], where $a = 0.246$ nm is the lattice constant of the monolayer graphene. At the full band filling, the superlattice carrier density, n_s , can be expressed as $n_s = 4/A = 8\theta^2/\sqrt{3}a^2$. Using this expression the twist angle, θ , is determined from the densities at the full band filling peaks (Figure. 2(a) of the main text and SI-Fig. 1c,d). In our case, for the superlattice, the peak densities are at $n \sim \pm 2.15 \times 10^{12}$ cm⁻², which gives a twist angle of $\theta \sim 0.95^{\circ}$. The calculated θ translates to a moiré wavelength of $\lambda_m \sim 14.47$ nm ($\sim a/\theta$).



SI-Fig. 1: Device optical image, response, and twist angle determination: **a)** Twisted bilayer graphene (tBLG) encapsulated with top and bottom hBN flakes deposited on SiO₂/Si substrate. The overlap area of the two twisted graphene layers is marked in dashed lines. The scale in the image is 5 μ m. **b)** Metal contacted device image of a standard Hall-bar with metallic top gate. The scale in the image is 2 μ m. **c)** Four probe resistances (R_{xx} vs ν) at $T = 5$ K and $D \sim 0.00$ V/nm between different contact probes marked as A, B, and C in (b). Apart from the peak at the charge neutrality point (CNP), two secondary peaks appear almost at the same value of number density, n , between different contact configurations indicating twist angle homogeneity in the device. **d)** Variation of R_{xx} with ν at 25 mK and at $D \sim 0.00$ V/nm for two pairs of contact configurations A-B and B-C. The value of the angle extracted from the secondary peaks is $\theta = 0.95^{\circ} \pm 0.02^{\circ}$. **e)** R_{xx} vs ν for various values of increasing temperature from 5 K up to 260 K ($D \sim 0.00$ V/nm) for contacts A-B measured in the first thermal cycle of the device.

SI-2: Controlling the number density, n , and the displacement field, D .

In this section, we discuss how we have tuned the electrostatic doping and the applied perpendicular displacement field in our measurements. The metallic layer on top of the top hBN and the SiO₂/Si act as the top gate and the global back gate, respectively. By sweeping the applied top gate (V_{tg}) and back gate (V_{bg}) voltages we can control the number density, n , and the vertical displacement field, D , in our device[13, 14, 15, 16, 17].

Controlling n :

$$n = \frac{C_{bg}(V_{bg} - V_{bg,0}) + C_{tg}(V_{tg} - V_{tg,0})}{e} \quad (1)$$

Controlling D :

$$D = \frac{C_{bg}(V_{bg} - V_{bg,0}) - C_{tg}(V_{tg} - V_{tg,0})}{2\epsilon_0} \quad (2)$$

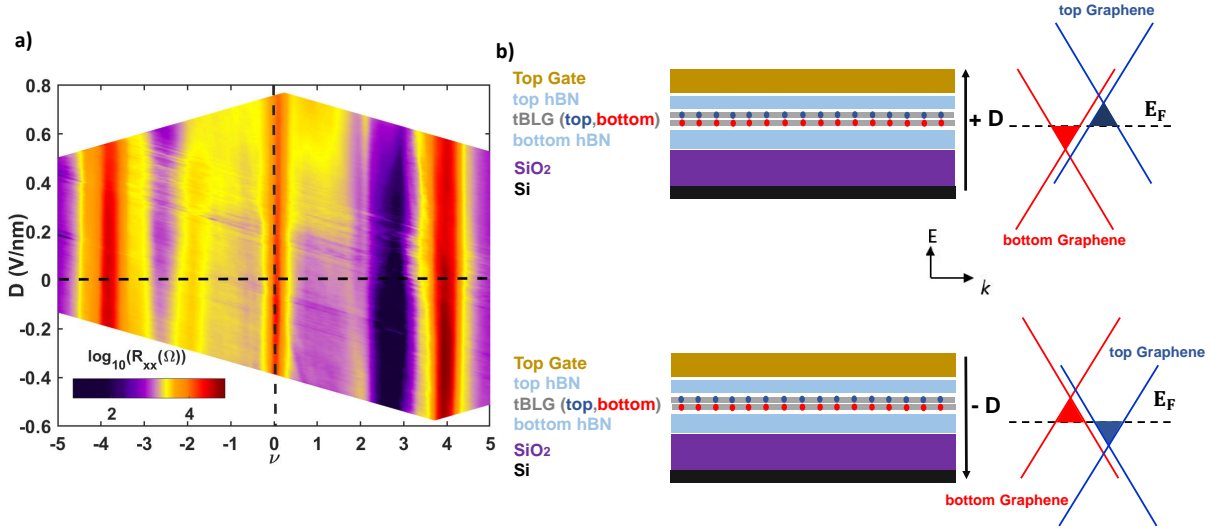
Here C_{bg} , C_{tg} , $V_{bg,0}$, $V_{tg,0}$, e and ϵ_0 are respectively the back gate capacitance per area, top gate capacitance per area, bottom gate voltage offset, top gate voltage offset, bare electronic charge, and free space (vacuum) permittivity. The thicknesses of the encapsulating top and bottom hBN layers are ~ 27 nm and ~ 30 nm, respectively.

SI-3: $\nu - D$ phase diagram from R_{xx} .

We have measured the longitudinal resistance, R_{xx} , between the contacts A-B by simultaneously changing V_{tg} and V_{bg} by use of a YOKOGAWA GS200 source meter and a Keithley 2400 source meter. The recorded $R_{xx}(V_{tg}, V_{bg})$ is converted to a $R_{xx}(\nu, D)$ colormap using equations (1) and (2) mentioned in SI-2 and as shown in SI-Fig. 2a. The superconductivity with low resistance on the electronic side (conduction band) and its tunability with $|D|$ are clearly seen.

Discussion on the asymmetric tunability of superconductivity with D : In this section, we discuss why the asymmetry is seen for positive and negative D . It can be seen that with $+D$ the superconductivity (observed for the electron doping) is more tunable than for $-D$. This asymmetry may arise from the different dielectric environments surrounding the tBLG. Referring to equation (2) (see SI-Fig. 2b), it is evident that $+D$ directs the electric field from the SiO₂/Si substrate towards the metal top gate, while $-D$ directs it from the metal top gate towards the SiO₂/Si substrate. The potential energy difference between the layers results in a shift in the Dirac cones of the individual layers as shown schematically in SI-Fig. 2b. For $+D$, the conduction band of the twisted bilayer graphene (tBLG) originates predominantly from the bottom graphene layer, while for $-D$, the top graphene layer contributes to the conduction band. However, the dielectric environments around the graphene layers are not identical. The bottom graphene layer is separated from the Si layer by the thicker (~ 30 nm) hBN layer and the SiO₂ dielectric (285 nm), whereas the top graphene layer is in closer proximity to the metallic top gate, separated only by the thinner hBN layer (~ 27 nm). Due to this asymmetry in the dielectric environment in our dual-gate structure, the polarizability

or screening response of the conduction band would be different for $+D$ and $-D$, which results in the asymmetric response seen in our results.



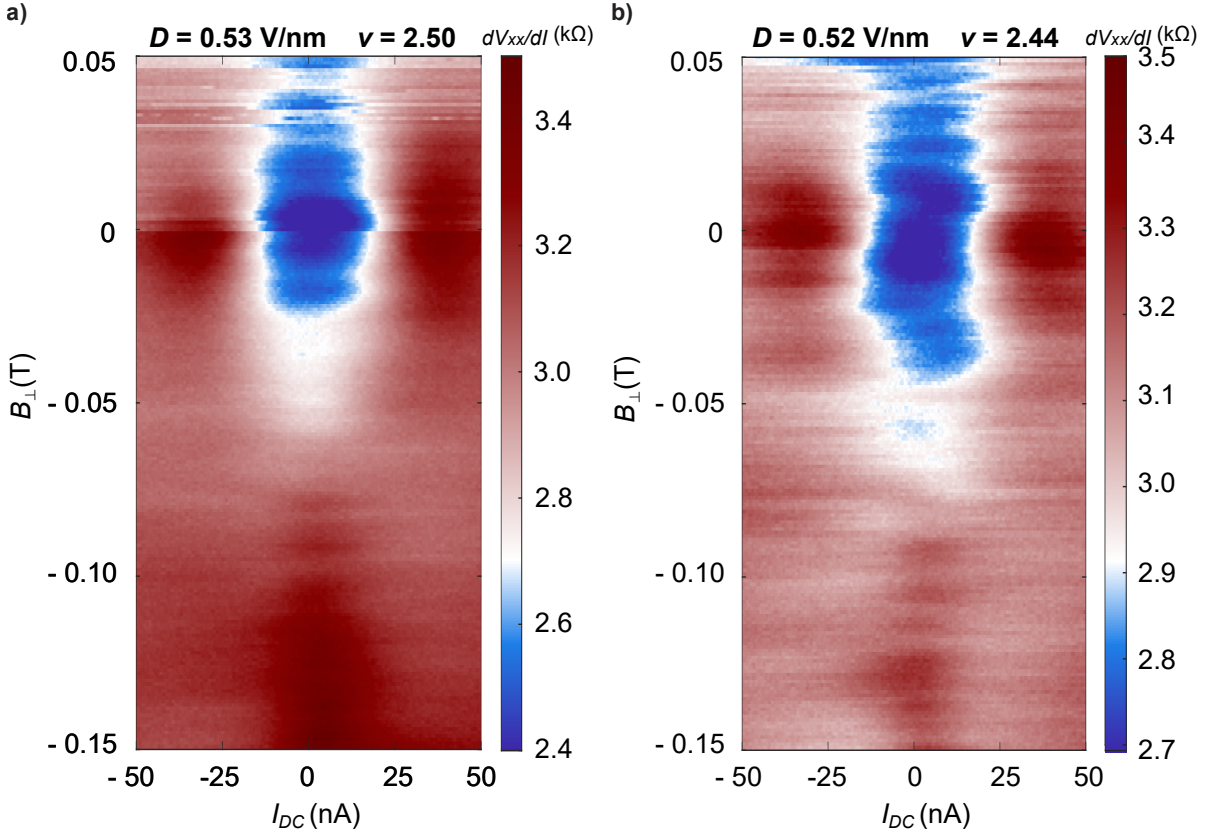
SI-Fig. 2: $\nu - D$ phase diagram of R_{xx} : **a)** R_{xx} phase map with ν and D at $T = 20$ mK. Superconductivity emerges between $\nu = 2$ and $\nu = 3$ on the electron side, as highlighted in dark purple color. A slight increase of resistance can be seen at $\nu = 2$ as we move towards higher values of $|D|$. **b)** Schematic of the dual-gate structure of the tBLG device. $+D$ points the electric field from SiO₂/Si substrate towards the metal top gate. Similarly, $-D$ points from the metal top gate towards the SiO₂/Si substrate. The right panels show the respective position of the band dispersion coming from the top and bottom layer graphene.

SI-4: Fraunhofer pattern at different D : signature of phase coherence in the SC phase.

2D superconductors show periodic oscillations of the critical bias current, I_c , and the differential resistance with varying applied magnetic field, B_{\perp} . This is a result of phase-coherent transport in Josephson junctions formed between the superconducting and insulating regions in the form of an array which is another hallmark of superconductivity in 2D systems [1]. We have measured dV_{xx}/dI with varying I_{DC} with the applied B_{\perp} ranging from -150 mT to 50 mT at different values of the ν and D in order to reveal the signature of phase coherence as demonstrated in Figure.2d (right panel) in the main text and SI-Fig. 3a,b. The period of oscillations is ~ 10 mT.

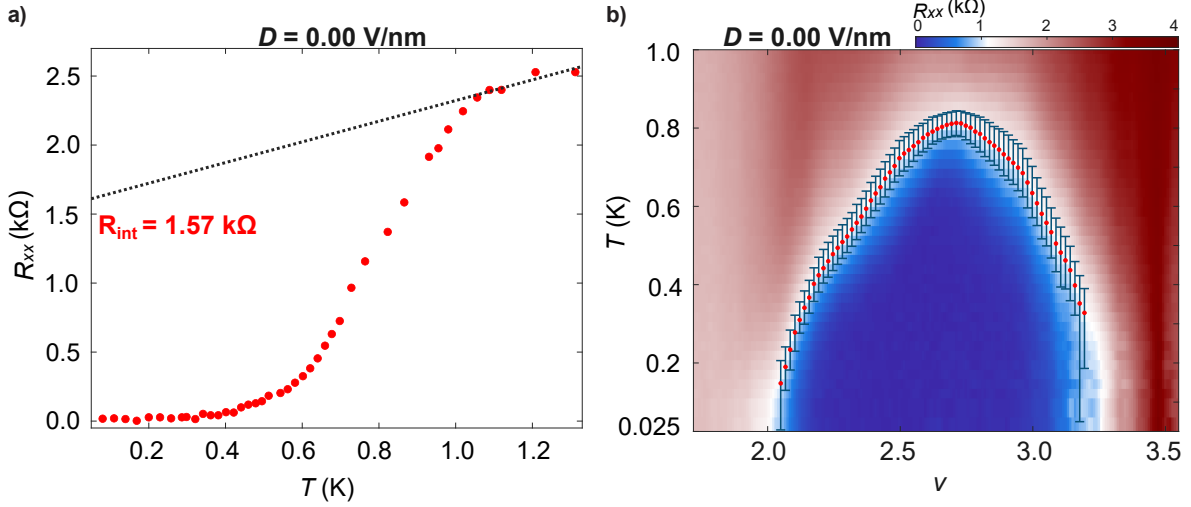
SI-5: Method of extraction of the superconducting critical temperature, T_c .

To determine the superconducting critical temperature, T_c , we employed the following method. SI-Fig 4a shows R_{xx} vs T plots for $D = 0.00$ V/nm from the lowest temperature measured in our system of ~ 25 mK up to 1.20 K. We fit the part where R_{xx} starts to saturate ($T \geq 0.9$ K) with a straight line and extrapolate



SI-Fig. 3: Fraunhofer oscillations: 2-d colormap of the differential resistance with B_{\perp} and the D.C bias current at $T = 25$ mK for **a)** $\nu, D = 2.50, 0.53$ V/nm ; and **b)** $\nu, D = 2.44, 0.52$ V/nm . The oscillation period in ΔB_{\perp} is ~ 10 mT and ~ 9 mT, respectively, which translates to an area of $0.206 \mu\text{m}^2$ and $0.229 \mu\text{m}^2$ respectively for the two chosen ν, D pairs.

the straight line to $T = 0$ K. The intercept (defined as R_{int}) on the R_{xx} axis at $T = 0$ K is considered as the resistance of the normal state, R_n . We define the superconducting critical temperature, T_c , as the temperature T at which R_{xx} drops to 50% of R_n .



SI-Fig. 4: Superconducting T_c determination: **a)** Increase of the resistance, R_{xx} , for $D \sim 0.00$ V/nm with temperature, T , showing the transition from the superconducting to the normal phase at $\nu \sim 2.7$. The intercept for the straight line that fits the higher temperature (≥ 0.9 K) part is labeled as R_{int} and identified as the normal state resistance, R_n . The temperature value for which R_{xx} becomes 50% of R_n is taken as the superconducting critical temperature, T_c . **b)** Fixed resistance contour ($\equiv 0.5R_n$) for T_c projected on the $R_{xx}(\nu, T)$ superconducting dome at $D = 0.00$ V/nm. The error bars correspond to the 60% and 40% thresholds of R_n .

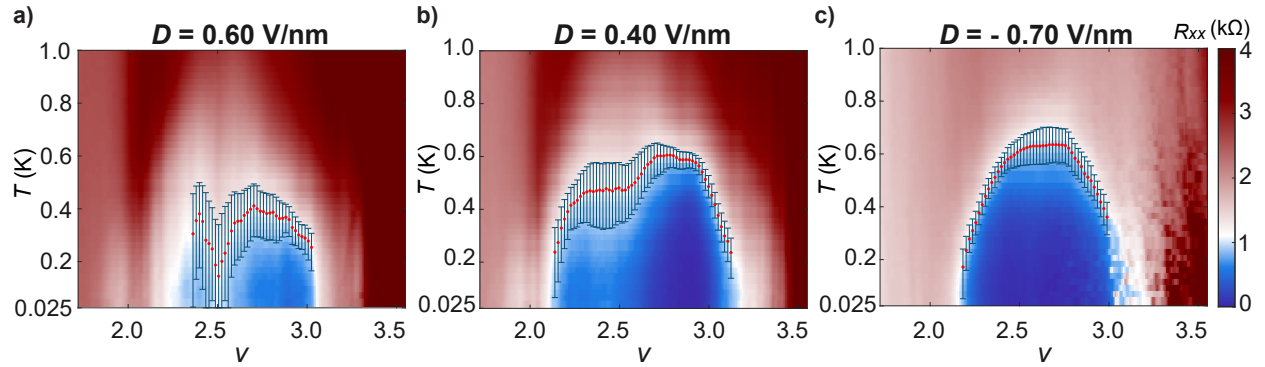
SI-6: Raw data related to superconductivity metrics.

I. $R_{xx}(\nu, T)$ superconductivity dome at different D :

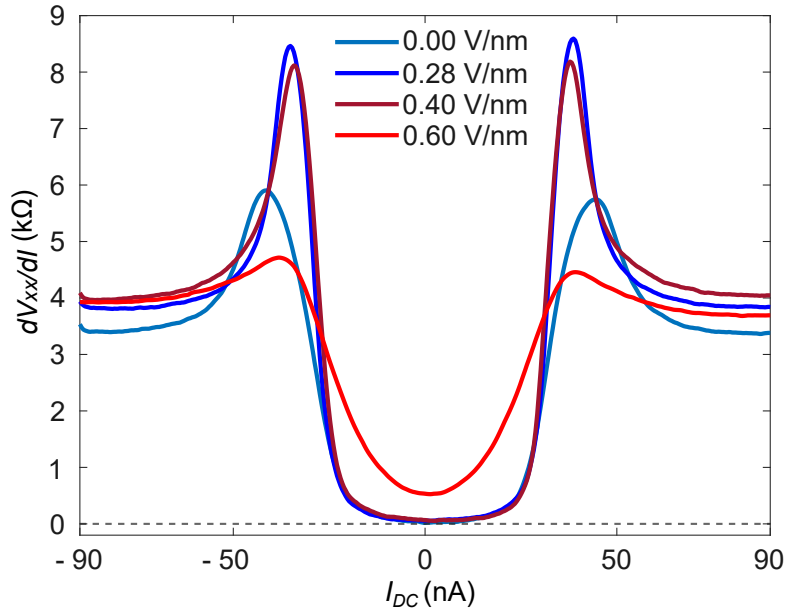
Similar to the SC dome structure shown in SI-Fig. 4b we have measured $R_{xx}(\nu, T)$ domes at other D values as shown in SI-Fig. 5 to see the evolution of the electron SC pocket as a function of D . The variation of T_c seen from these domes is shown in Figure. 4a in the main text.

II. dV_{xx}/dI vs I_{DC} for different values of D :

The weakening/suppression of the SC phase with $|D|$ gets reflected in the gradual decrement of the critical DC bias current, I_c , as shown in Figure. 4b in the main text. SI-Fig. 6 shows the measured dV_{xx}/dI vs I_{DC} at a few selected D fields. The value of $|I_{DC}|$ where dV_{xx}/dI peaks is taken as I_c for a given D .



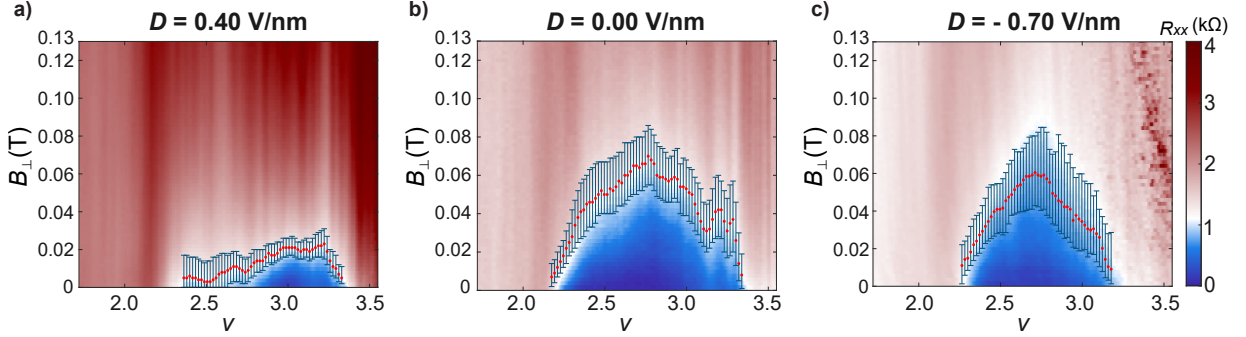
SI-Fig. 5: $R_{xx}(\nu, T)$ SC dome at different D : 2-d colormap of R_{xx} with ν and T for the following D values: **a)** 0.60 V/nm, **b)** 0.40 V/nm, and **c)** -0.70 V/nm. Variation of T_c vs ν can be seen from the projected fixed resistance contour (red dots $\equiv 0.5R_n$) at these D fields. The error bars correspond to the 60% and 40% thresholds of R_n .



SI-Fig. 6: Critical D.C. bias current, I_c , for different D : Differential resistance is plotted against I_{DC} for different D values. The decrement of I_c values with D is apparent from the shift in the peak positions in I_{DC} .

III. $R_{xx}(\nu, B_{\perp})$ superconductivity dome at different D :

$R_{xx}(\nu, B_{\perp})$ SC domes at different D values are shown in SI-Fig. 7 to see the evolution of the electron SC pocket at different D as well as to quantify the change in $B_{c\perp}$. The variation of $B_{c\perp}$ as seen from these domes is shown in Figure. 4c in the main text.



SI-Fig. 7: $R_{xx}(\nu, B_{\perp})$ SC dome at different $\nu - D$: 2-d colormap of R_{xx} with ν and B_{\perp} at 25 mK for the following D values: **a)** 0.40 V/nm, **b)** 0.00 V/nm, and **c)** -0.70 V/nm. Variation of $B_{c\perp}$ can be seen from the projected fixed resistance contour (red dots $\equiv 0.5R_n$) at these D fields in a similar spirit to the determination of T_c from the $R_{xx}(\nu, T)$ domes in SI-Fig. 5. The error bars correspond to the 60% and 40% thresholds of R_n .

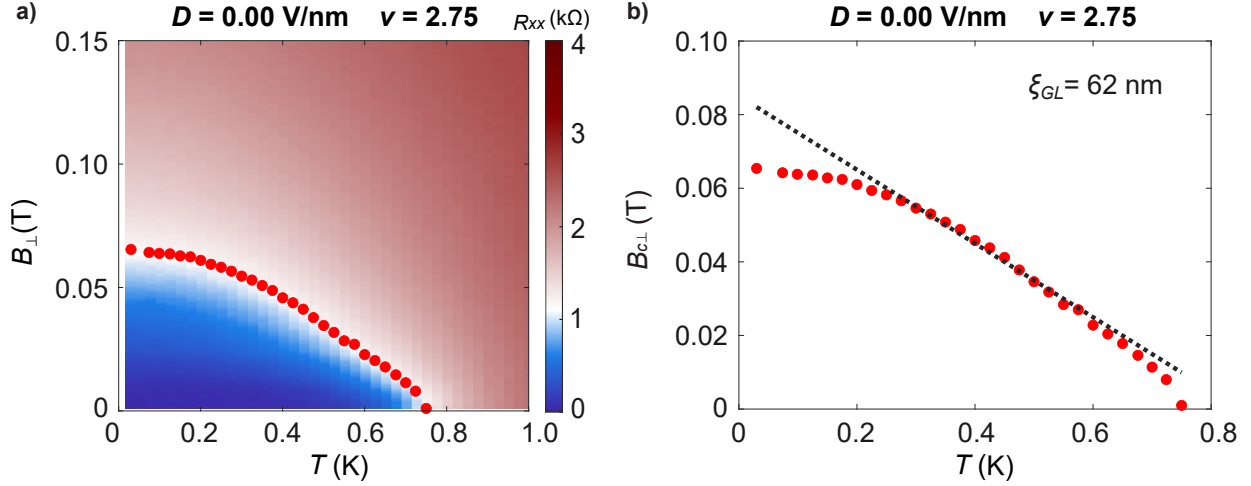
IV. Ginzburg-Landau coherence length (ξ_{GL}):

From Ginzburg-Landau theory, we can get the dependence of the perpendicular critical magnetic field, $B_{c\perp}$, on temperature which is given by [18] -

$$B_{c\perp} = \frac{\phi_0}{2\pi\xi_{GL}^2} \left(1 - \frac{T}{T_c}\right) \quad (3)$$

where $\phi_0 = h/(2e)$ is the superconducting magnetic flux quantum, h is the Planck's constant, T_c is superconducting critical temperature (for a given D) and ξ_{GL} is the superconducting coherence length. In SI-Fig. 8, we have shown how ξ_{GL} is extracted from the $R_{xx}(T, B_{c\perp})$ plot. For ν, D and in the superconducting phase, we measure R_{xx} for different values of T and B_{\perp} to generate the T, B_{\perp} phase diagram for a given strength of the SC phase. Using the resistance threshold of $0.5R_n$ as described in SI-5 we can extract the critical perpendicular magnetic field, $B_{c\perp}$, at each measured T . The result is a plot shown in SI- Fig. 8b which can be fitted to equation (3) to extract the $T = 0$ K limit of the critical perpendicular magnetic field, $B_{c\perp}^0$ (through the intercept on the $B_{c\perp}$ axis). The GL coherence length for the measured ν, D is then given as -

$$\xi_{GL} = \left(\frac{\phi_0}{2\pi B_{c\perp}^0}\right)^{1/2} \quad (4)$$



SI-Fig. 8: ξ_{GL} extraction: **a)** R_{xx} colormap of the SC phase at $D = 0.00$ V/nm and $\nu = 2.75$ with T and B_{\perp} . Values of the critical perpendicular magnetic field, $B_{c\perp}$, at each temperature, are marked by red solid circles. **b)** The $B_{c\perp}$ at different T is fitted with a straight line to the Ginzburg - Landau expression (equation (3)) to extract the inferred $T = 0$ K limit of the critical perpendicular magnetic field, $B_{c\perp}^0$. The extracted value of GL coherence length (ξ_{GL}) is $\simeq 62$ nm.

V. $B_{c\parallel}$ and Pauli limit (B_P): implication, measurement, and calculation.

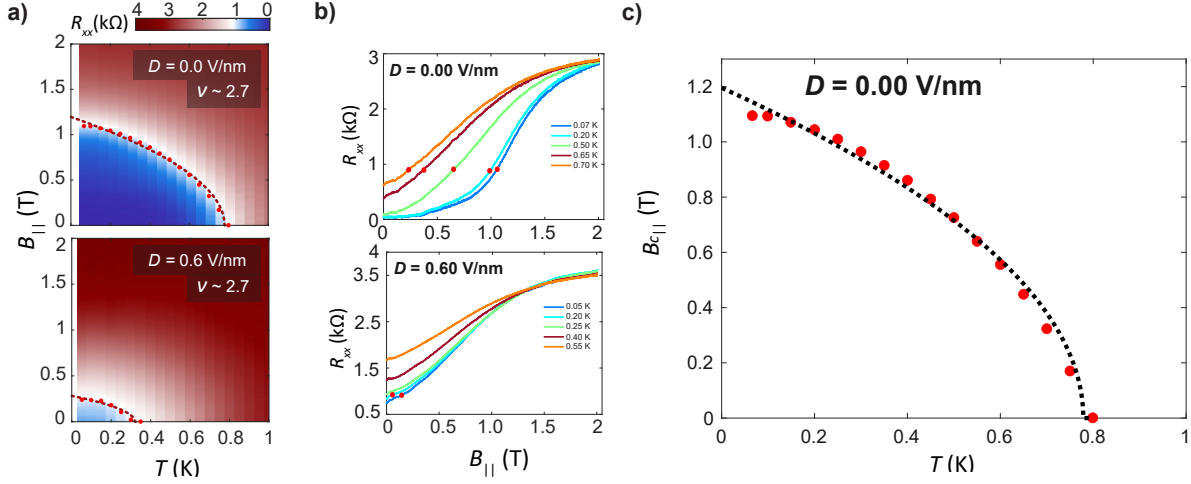
In this section, we discuss the effect of the in-plane or parallel magnetic field, B_{\parallel} , in a conventional two-dimensional superconductor. In the limit of BCS theory a superconductor with spin-singlet Cooper pairs is split when the Zeeman energy induced by the in-plane magnetic field exceeds the superconducting pairing gap, $\Delta = 1.76k_B T_c$ [18], where k_B is the Boltzmann constant. The in-plane magnetic field limit for such weakly coupled superconductors is known as the Pauli (or Clogston–Chandrasekhar) limit [19, 20] which can be written as $B_P = 1.76k_B T_c^0 \sqrt{2}/g\mu_B$ [14] and gives $B_P = 1.86$ Tesla/K $\times T_c^0$ for a Landé g-factor (g) of 2. Empirically, the temperature dependence of the in-plane critical magnetic field, $B_{c\parallel}$, is as follows [21]-

$$B_{c\parallel} \propto \left(1 - \frac{T}{T_c^0}\right)^{1/2} \quad (5)$$

where T_c^0 is superconducting critical temperature at $B_{\parallel} = 0$ T (for a given D).

For different values of D at $\nu_{optimal}$ in the SC phase, we measure a R_{xx} at discrete set of temperatures, T , while continuously tuning the applied B_{\parallel} (SI-Fig. 9a). The resistance threshold of $0.5R_n$ as described in SI-5 gives the values for the critical in-plane magnetic field, $B_{c\parallel}$ (SI-Fig. 9b), at each T in the form of a fixed resistance contour for $T - B_{c\parallel}$ (SI-Fig. 9c). The contour at each such ν, D choice is fitted to $T/T_c^0 = 1 - \alpha(B_{c\parallel})^2$ [1, 3, 20, 22], where α is a fitting parameter and at the inferred $T = 0$ K limit $1/\sqrt{\alpha} = B_{c\parallel}^0$,

zero temperature critical in-plane magnetic field. We have found that in our measured tBLG device, for a given D , $B_{c\parallel}^0$ is less than the expected value of the Pauli limit, B_P (for $D = 0.00$ V/nm $B_P \simeq 1.48$ T and $B_{c\parallel}^0 \simeq 1.2$ T), confirming the conventional weakly-coupled nature of the superconductivity in tBLG.



SI-Fig. 9: $B_{c\parallel}^0$ extraction: **a)** R_{xx} with B_{\parallel} and T for zero D (top panel) and 0.60 V/nm (bottom panel). The temperature dependence of $B_{c\parallel}$ (red circles) is fitted (dashed black line) to extract the critical parallel magnetic field at zero temperature, $B_{c\parallel}^0 \sim 1.2$ T and 0.3 T for $D = 0.00$ V/nm and 0.60 V/nm, respectively at $\nu \sim 2.7$, which matches well with the Pauli limit calculated from the zero magnetic field T_c^0 , $B_p = 1.76k_B T_c^0 \sqrt{2}/g\mu_B$. **b)** Line plots of R_{xx} vs B_{\parallel} for $D = 0.00$ V/nm (top panel) and 0.60 V/nm (bottom panel) with increasing T . The red circles are the points with resistance values $\simeq 0.5R_n$. **c)** Fixed resistance ($\equiv 0.5R_n$) contour points in red circles in $T - B_{c\parallel}$. The dashed black curve is fit to the points by using $T/T_c^0 = 1 - \alpha(B_{c\parallel})^2$, where $T_c^0 \sim 0.8$ K for $D = 0.00$ V/nm. From the fit $B_{c\parallel}^0 \simeq 1.2$ T for $D = 0.00$ V/nm.

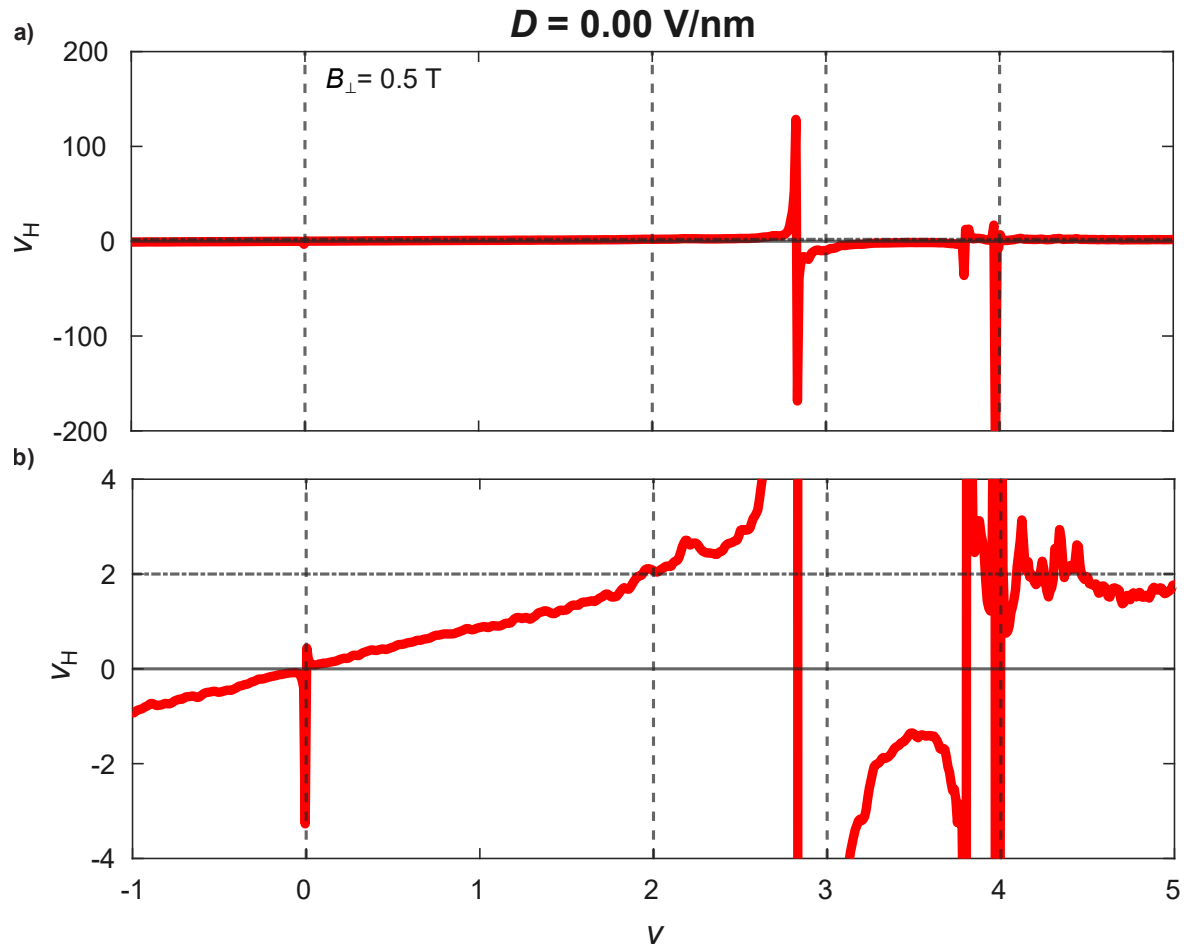
SI-7: R_{xy} and Hall filling, ν_H .

I. Anti-symmetrization of R_{xy} :

The transverse resistance, R_{xy} , used here is anti-symmetrized to avoid the contribution due to the possible asymmetric position of the transverse contacts. The anti-symmetrization is done as follows -

$$R_{xy}^{anti-symm} = R_{xy} = \frac{R_{xy}(+B_{\perp}) - R_{xy}(-B_{\perp})}{2} \quad (6)$$

where, $|B_{\perp}| = 0.5$ T.



SI-Fig. 10: ν_H vs ν : **a)** ν_H vs ν at $D = 0.00$ V/nm. Divergence in ν_H (position of vHs) is reflected in high values of $|\nu_H|$ (≥ 200). **b)** Zoomed in plot of ν_H in the range ± 4 showing the change in carrier sign across CNP and divergences (vHs) at $\nu \sim 2.7$ and $\nu \sim 4$.

II. Definition of Hall filling, ν_H :

$$\nu_H = \frac{4n_H}{n_s} = \frac{4|B_\perp|}{eR_{xy}n_s} \quad (7)$$

where, $n_H = |B_\perp|/eR_{xy}$ is the Hall density, e is the bare electronic charge, and n_s is the full band filling number density or the position of the secondary peaks in R_{xx} on the n axis. Whenever R_{xy} becomes zero, ν_H diverges giving us insight into the van Hove singularities (vHs) in the band structure or the filling landscape. SI-Fig. 10 shows the ν_H vs the filling, ν , for $D = 0.00$ V/nm (at $|B_\perp| = 0.5$ T). Large divergences in ν_H are seen near $\nu \sim 2.7$ and $\nu \sim 4.0$. Divergence/vHs at $\nu \sim 2.7$ directly coincides with the position of the SC phase as shown in the main text in Figure. 5b,d.

SI-8: $\nu - D$ phase diagram of normalized Hall density (Hall filling) ν_H .

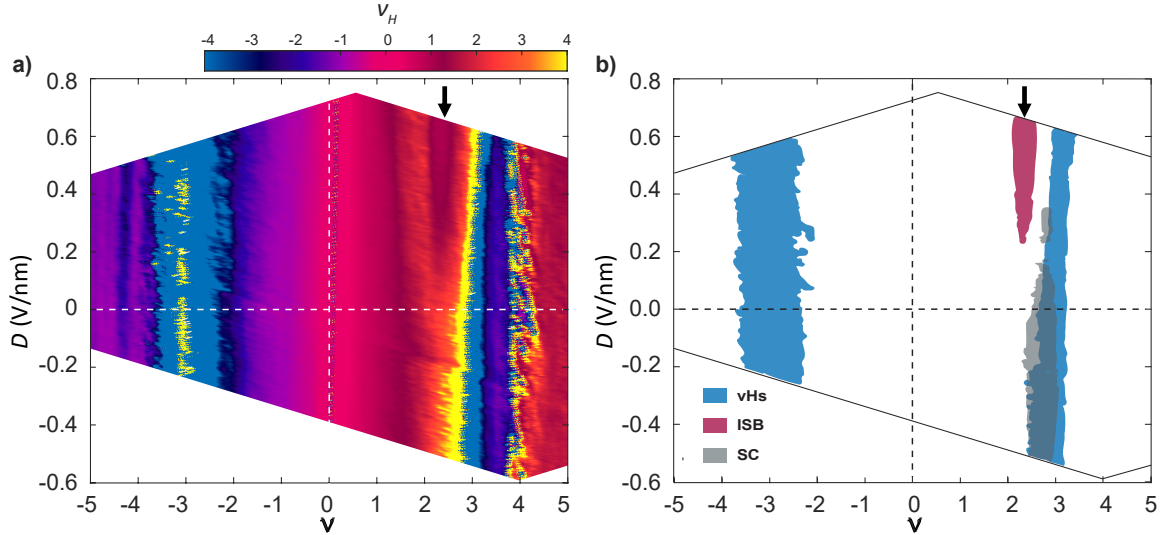
Similarly to the $\nu - D$ map of R_{xx} mentioned in SI-3 (SI-Fig. 2a), we have measured the transverse resistance, $R_{xy}(+B_\perp)$, and $R_{xy}(-B_\perp)$, between contacts B-D (SI-Fig. 1b) by simultaneously changing the V_{tg} and V_{bg} at $|B_\perp| = 0.5$ T. The anti-symmetrized (equation (6)) $R_{xy}(V_{tg}, V_{bg})$ converted to a $\nu_H(\nu, D)$ colormap using equations (1), (2), and (7) is shown in SI-Fig. 11a. SI-Fig. 11b shows a cartoon ν, D map with all the phases, i.e superconductivity (SC), isospin broken symmetry (ISB), and vHs projected according to the regions in ν and D where they appear in SI-Fig. 2a and SI-Fig. 11a.

SI-9: σ_{xx} Landau level Fan Diagram.

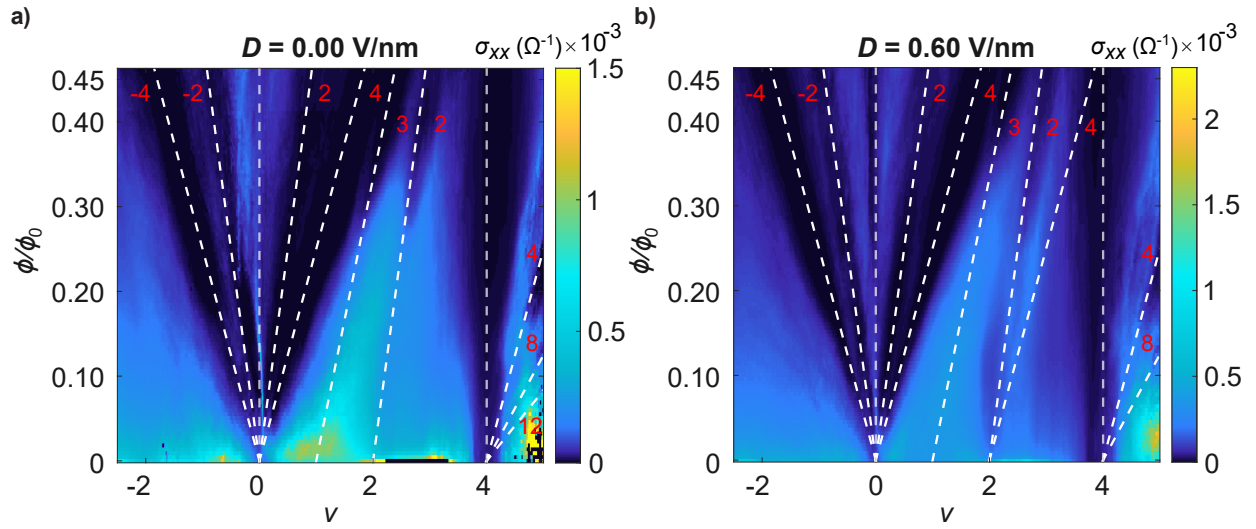
The longitudinal conductivity, σ_{xx} , in a device with a Hall-bar geometry is expressed as [23]-

$$\sigma_{xx} = \frac{(\frac{W}{L})R_{xx}}{(\frac{W}{L})^2R_{xx}^2 + R_{xy}^2} \quad (8)$$

where W and L are the designated width and length of the device while measuring the longitudinal resistance, R_{xx} . L is the distance between the respective Hall probes used to measure R_{xx} and W is the transverse length covered by the top gate. R_{xy} is the measured transverse resistance. R_{xx} and R_{xy} are measured simultaneously by tuning the number density, n , in our device in the presence of B_\perp up to 10 T for zero D (0.00 V/nm) and in the high displacement field regime (0.60 V/nm). Measured R_{xx} and R_{xy} is converted to σ_{xx} using equation (8). The formation of Landau levels in the presence of applied strong magnetic fields (B_\perp , up to 10 T) is shown in SI-Fig. 12 for $D = 0.00$ V/nm and 0.60 V/nm. We can identify the visible fan lines emanating from different filling integer factors, $\nu(0, 1, 2, 4)$, in the Wannier diagram (linear trajectories in $\nu, \phi/\phi_0$ phase space) [24] using the Diophantine relation: $\nu = N\phi/\phi_0 + s$ [2, 17, 23, 25, 26, 27], where $\phi = B_\perp A$ is the magnetic flux penetrating through a moiré unit cell, $\phi = h/e$ is the magnetic flux quantum, $\nu(\equiv 4n/n_s)$, N are integers and $s = 0$ gives the main Landau fan, $s = \pm 1$ is the first satellite fan on either side of CNP and so on [2].



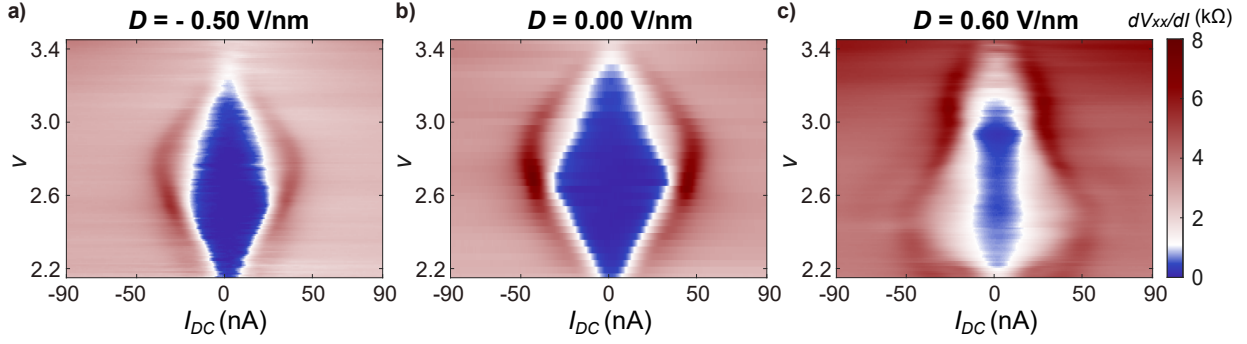
SI-Fig. 11: Normalized Hall density ν_H vs D : **a)** Normalized Hall density or Hall filling, ν_H ($\frac{4|B_\perp|}{eR_{xy}n_s}$), plotted as a function of ν and D for $|B_\perp| = 0.5$ T and $T = 25$ mK. The vHs appears on the electron side at around $\nu \sim 2.7$ for $D \sim 0.00$ V/nm. The vHs at $\nu \sim 2.7$ migrates towards $\nu \sim 3$ with increasing +ve D . For $D \geq +0.20$ V/nm the change in slope in ν_H vs ν as seen in Figure. 5f in the main text can be seen from the change in the color gradient around $\nu \sim 2$ marked by a black arrow (\downarrow). The reduction of sudden Hall density (filling) is due to the broken isospin-symmetry (ISB) with increasing D . Indication of rapid sign changes with large divergences (vHs) can also be seen on the hole side centered around $\nu \sim -3$ for the whole range of accessible D . **b)** Schematic of the D dependent phases with filling factor, ν , observed in our tBLG device. We have used three different colors to mark the overlapping region of superconductivity (grey), vHs (blue), and the regions of Hall density (filling) reduction marked as ‘ISB’ for the isospin symmetry breaking phase (magenta) also marked by a black arrow (\downarrow) similar to in **(a)**. The ‘ISB’ phase bounds the two phases (SC and vHs) on the left side of the $\nu - D$ diagram for $D \geq +0.20$ V/nm centered around $\nu \sim 2$.



SI-Fig. 12: Fan diagram: Landau fan diagrams for **a)** $D = 0.00$ V/nm and **b)** $D = 0.60$ V/nm. Applied B_{\perp} (up to 10 T) is converted to ϕ/ϕ_0 , where $\phi = B_{\perp}A$, A is the area of the superlattice unit cell, $\phi_0 = h/e$ is the magnetic flux quantum, h is the Planck's constant, and e is the bare electronic charge. Visible fan lines (Wannier diagram) emanate from $\nu = 0$ and ± 4 for both values of the D . Fan lines with sequence $N = +2, +4$ (from the Diophantine relation mentioned in SI-9) emerge from $\nu = 2$ at $D = 0.60$ V/nm in comparison to a single line of $+2$ at 0.00 V/nm pointing towards a degeneracy reduction from $g_d = 4$ to $g_d = 2$ for higher D regime.

SI-10: Differential resistance vs ν at different D .

In this section, we discuss another way by which we see the evolution of the electron SC pocket with the application of D in the filling range of $2 \leq \nu \leq 3$. SI-Fig. 13 shows the colormaps of the differential resistance measured as a function of the D.C bias current, I_{DC} , and the filling factor, ν , at three different representative displacement fields, $-ve$ $D(-0.50$ V/nm), neutral $D(0.00$ V/nm), and $+ve$ $D(0.60$ V/nm).



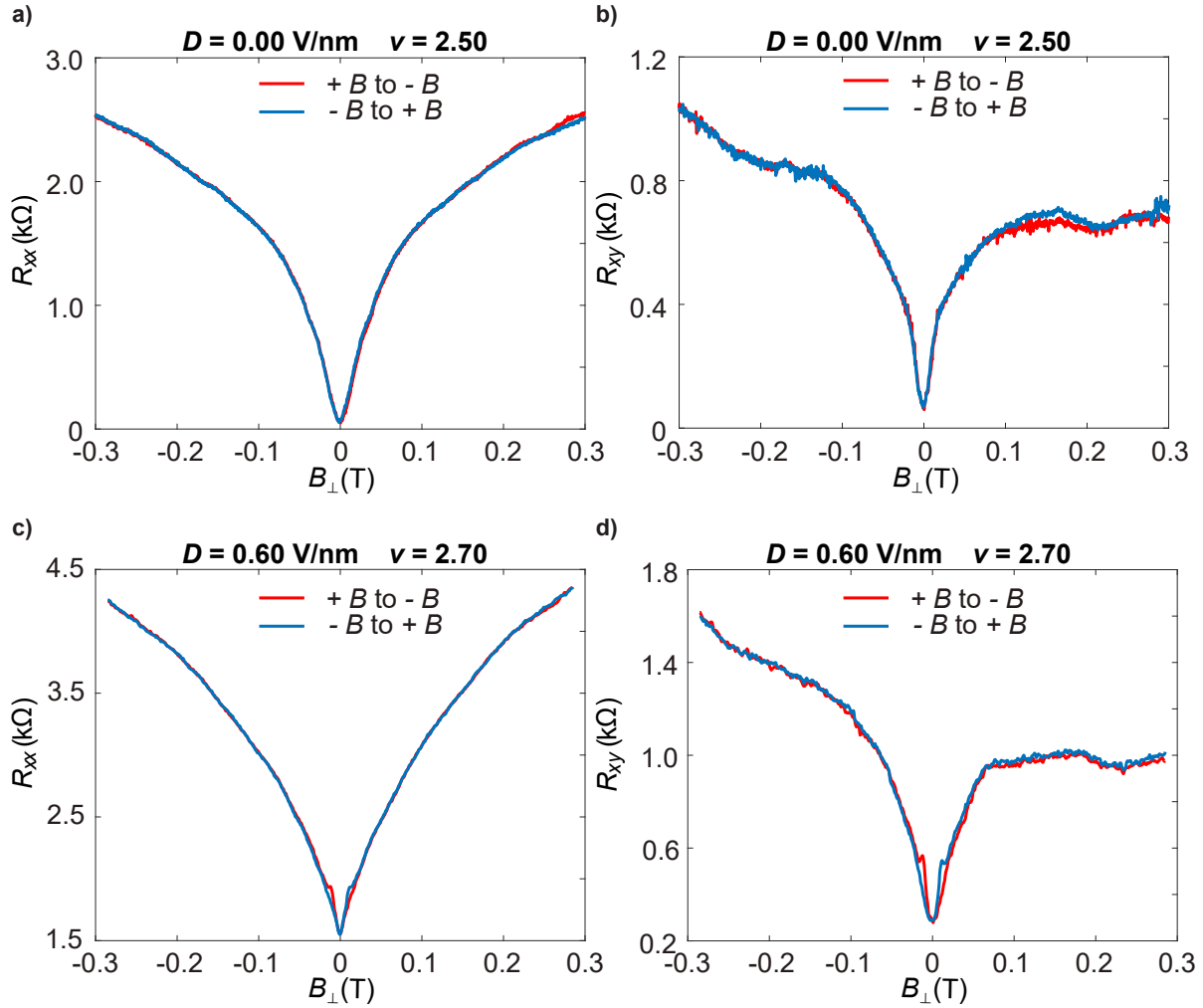
SI-Fig. 13: $dV_{xx}/dI(\nu, I_{DC})$ at different D : To showcase the variation of superconductivity with $+ve$ and $-ve$ displacement fields, D , we have plotted dV_{xx}/dI vs ν and I_{DC} at the following D values : **a)** -0.50 V/nm, **b)** 0.00 V/nm, and **c)** 0.60 V/nm, with ν being tuned across the SC region. The shift in the optimal doping point, $\nu_{optimal}$, with the application of D across 0.00 V/nm is evident from the 2-d colormaps.

SI-11: Looking for possible magnetic structures: Hysteresis with B_{\perp} .

The signature of magnetic structures like anomalous Hall effect [28], orbital ferromagnetism in tBLG [29, 30] and other twisted systems like twisted double bilayer graphene (TDBLG) [15] has reportedly been observed in the form of hysteresis in resistance in the presence of the applied magnetic field. The possibility of the tuning of the superconductivity with D in our device being due to the presence of magnetic structures (magnetism) is ruled out in the hysteresis experiment at zero D and symmetry broken high D regime by sweeping B_{\perp} . We do not see any sign of hysteresis in either R_{xx} or R_{xy} (see SI-Fig. 14) confirming the absence of any magnetism as well as anomalous Hall behavior in our device.

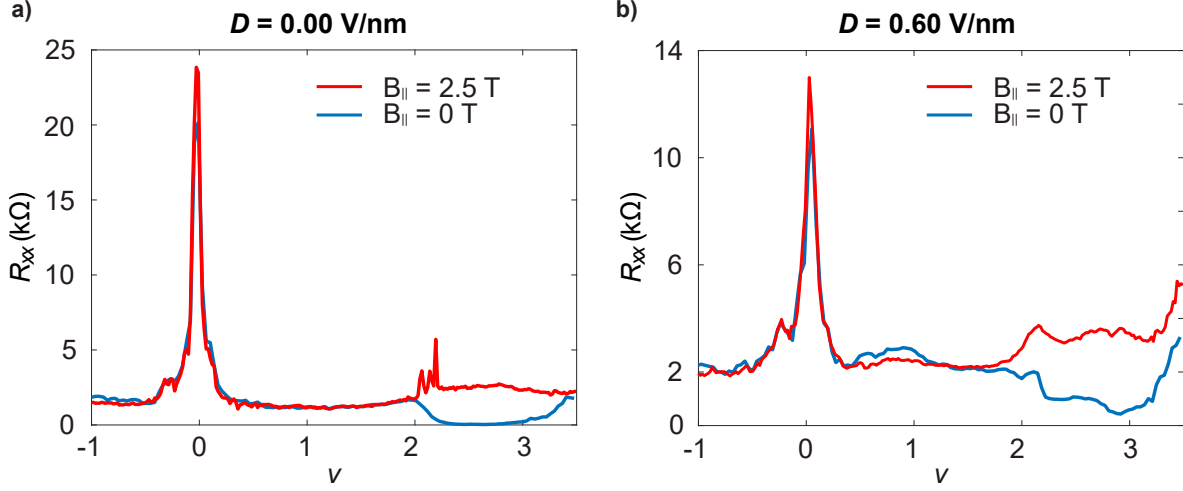
SI-12: R_{xx} in B_{\parallel} .

In section SI-6(V) we have seen how an in-plane magnetic field affects the superconducting phase by splitting the Cooper pairs for magnetic fields above the Pauli limit, B_P . R_{xx} vs ν at two different values of B_{\parallel} is shown in SI-Fig. 15, where we see the appearance of a resistance peak after the SC phase gets killed by the application of an in-plane magnetic field exceeding the B_P for $D = 0.00$ V/nm and 0.60 V/nm. In our tBLG device, at $B_{\parallel} = 0$ T there is no signature of correlation peak at zero D , though we see a finite resistance increase at $\nu \sim 2$ with the application of D as shown in Figure. 3a in the main text. As discussed in the main text, the weakening of superconductivity with D is likely connected to the flavor polarization of



SI-Fig. 14: Absence of magnetic structures: a) R_{xx} , and b) R_{xy} for two sweep directions ($+B_{\perp}$ to $-B_{\perp}$) and ($-B_{\perp}$ to $+B_{\perp}$) in the range of $B_{\perp} = \pm 300$ mT (ramp rate ~ 10 mT/min) at $\nu, D = 2.5, 0.00$ V/nm. The resistance values are almost similar, with no sign of hysteresis. c) R_{xx} , and d) R_{xy} for $\nu, D = 2.7, 0.60$ V/nm also show similar behavior. Here the ramp rate for the magnetic field is ~ 100 mT/min. The small kinks seen in the R_{xx} and R_{xy} could be due to a finite change in temperature of the sample stage due to the higher ramp rate of the superconducting magnet in the dilution fridge.

bands due to symmetry breaking near $\nu \sim 2$. Apart from the SC getting killed with B_{\parallel} and the appearance of resistance peak around $\nu \sim 2$, we do not see any signature of magnetic effects (with B_{\parallel}) in our device.



SI-Fig. 15: R_{xx} in a finite B_{\parallel} : Appearance of the resistance peak around $\nu \sim 2$ after killing off the SC phase by the application of an in-plane magnetic field exceeding the Pauli limit (B_P) for **a)** $D = 0.00$ V/nm, and **b)** 0.60 V/nm .

SI-13: Experimental signature of Charge density wave (CDW) order .

SI-Fig. 16 shows the difference in the evolution of R_{xx} with ν and B_{\perp} for $D = 0.00$ V/nm and 0.40 V/nm. SI-Fig. 16a shows a well developed $R_{xx}(\nu, B_{\perp})$ SC dome for zero D . SI-Fig. 16b shows line plots of R_{xx} vs ν for a few representative B_{\perp} values. Once SC is destroyed for $B_{\perp} > 90$ mT, we see signatures of weakly developed oscillations in R_{xx} as a function of ν . As can be seen in SI-Fig. 16c,d this effect is much more pronounced at $D = 0.40$ V/nm where the SC already has a diminished strength to begin with. R_{xx} shows well-pronounced oscillations that are periodic in ν suggesting the existence of the charge density wave (CDW) order with an estimated period of $\Delta\nu \sim 1/10$. The same can be confirmed by the dominant frequency, f_{CDW} , from the Fourier spectrum of the R_{xx} oscillations as shown in SI-Fig. 17b as $\Delta\nu \simeq 0.112$ for $D = 0.40$ V/nm. The above-mentioned period in filling can be converted into a change in number density, $\Delta n \simeq 0.06 \times 10^{12} \text{ cm}^{-2}$.

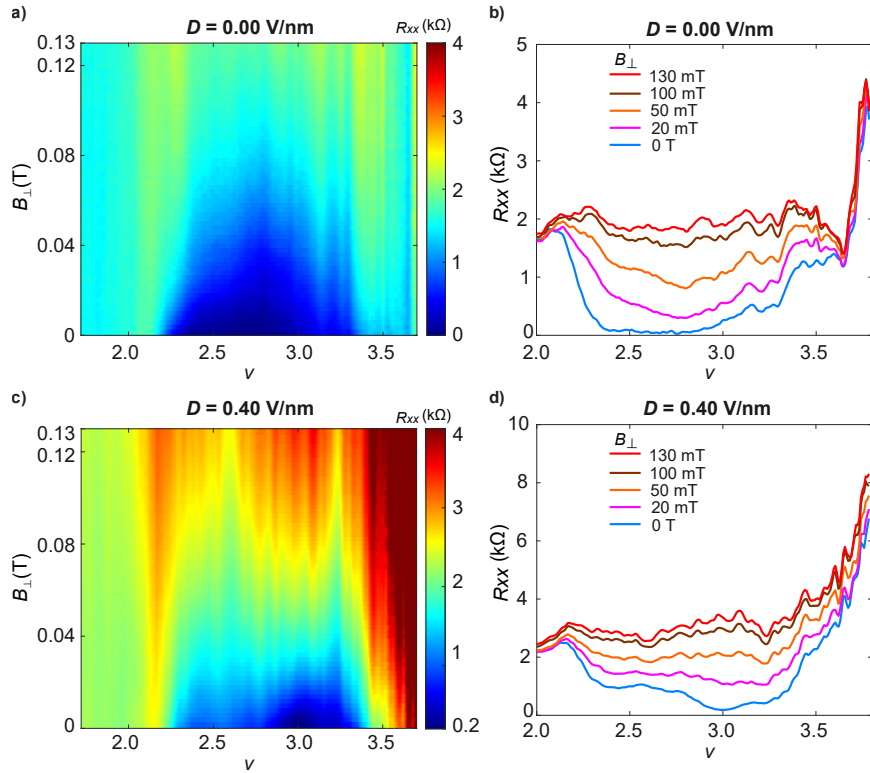
In 2D, the relation between the Fermi wave vector (\mathbf{k}_F) and number density (n) can be written as -

$$k_F = \sqrt{\pi n} \quad (9)$$

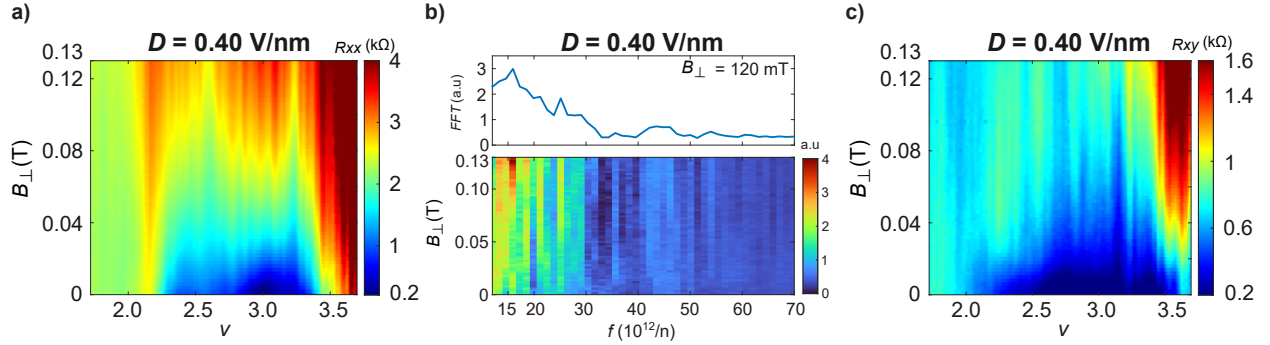
From the measured Δn using the above equation we get $\Delta k_F \simeq 4.34 \times 10^5 \text{ cm}^{-1}$. As discussed in SI-I, for our device with $\theta \sim 0.95^\circ$ the moiré wavelength is $\lambda_M \simeq 14.47 \text{ nm}$ and moiré wave vector is around $k_M \simeq 4.34 \times 10^6 \text{ cm}^{-1}$. Thus, from the estimated values of Δk_F and k_M , we have $\Delta k_F/k_M \sim 0.10$.

As shown in Figure. 6c of the main text, the theoretically calculated magnitude of the Fermi nesting vector $\Delta\mathbf{q}$ for $\nu, D = 1.6, 0.40$ V/nm, is around $(1/10)^{th}$ of the moiré Brillouin zone wave vector \mathbf{k}_{mBZ} which matches well with our experimental observations for $D = 0.40$ V/nm. In SI-Fig. 17c, we see similar oscillations in R_{xy} .

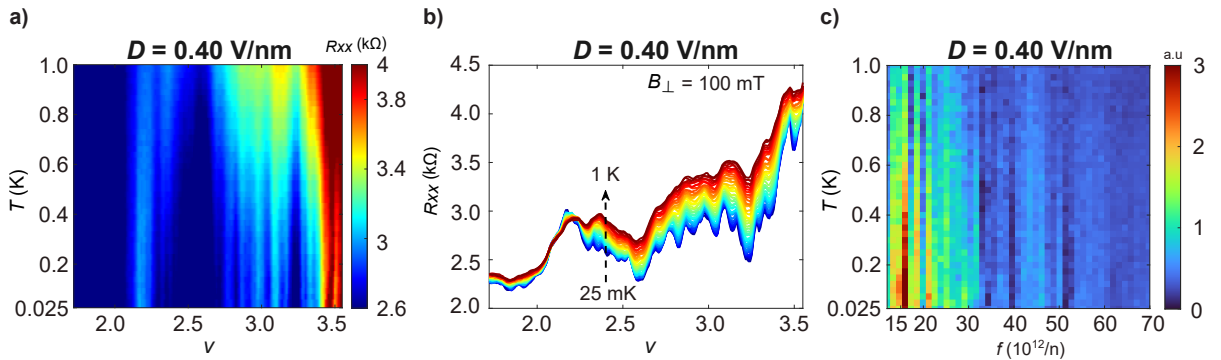
SI-Fig. 18 demonstrates the collapse of the CDW phase with increasing T at $D = 0.40$ V/nm. The temperature scale beyond which the oscillations start disappearing (T_c^{CDW}) is similar to the T_c for 0.40 V/nm (~ 0.6 K). SI-Fig. 19a shows a more well-developed CDW phase for $D = 0.60$ V/nm at the threshold of complete destruction of the SC phase due to D . We also see a small increase in the oscillation frequency with an oscillation period of $\Delta\nu \simeq 0.107$ ($f \propto 1/\Delta\nu$) for $D = 0.60$ V/nm as shown in SI-Fig. 19c. Similar CDW instabilities competing with the superconducting phase at finite D have already been reported in twisted trilayer graphene below the magic angle [31].



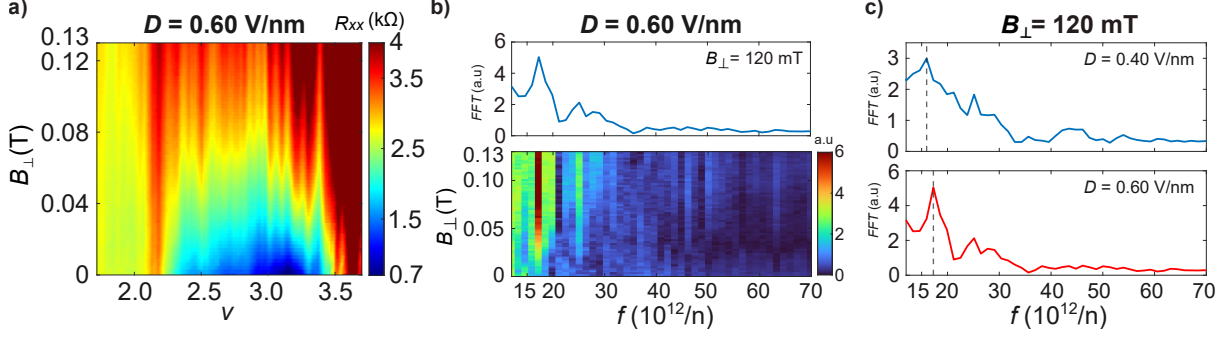
SI-Fig. 16: Competition between SC and CDW: **a)** $R_{xx}(\nu, B_{\perp})$ colormap as a function of ν and B_{\perp} showing the SC dome at $D = 0.00$ V/nm. **b)** R_{xx} vs ν line plots for $B_{\perp} = 0$ T, 20 mT, 50 mT, 100 mT and 130 mT at $D = 0.00$ V/nm. Weakly developed oscillations are seen for $\sim 2.7 < \nu < 3.3$ for $B_{\perp} > 50$ mT. **c)** $R_{xx}(\nu, B_{\perp})$ colormap at $D = 0.40$ V/nm with clear signatures of periodic oscillations in R_{xx} . **d)** Line plots for $B_{\perp} = 0$ T, 20 mT, 50 mT, 100 mT and 130 mT at $D = 0.40$ V/nm. The oscillations in R_{xx} with ν ($2.2 < \nu < 3.3$) reveals a period of $\Delta\nu \sim 1/10$.



SI-Fig. 17: CDW at higher D regime: **a)** Periodic oscillations in R_{xx} vs ν can be seen of 2-d colormap of R_{xx} vs ν, B_{\perp} for $D = 0.40$ V/nm at $T = 25$ mK for $B_{\perp} > 60$ mT. **b)** (bottom panel) 2-d colormap of the Fourier spectrum of **(a)**. The top panel shows the cut line for $B_{\perp} = 120$ mT with a 3-point running average. The x-axis (frequency) is plotted in normalized units of $10^{12}/n$ ($f = f_{actual}/2\pi; f_{actual} = 2\pi/n$) where n is the charge carrier number density. The dominant frequency, f_{CDW} , translates to an oscillation period of $\Delta\nu \simeq 0.112 (\sim 1/10)$. **c)** $R_{xy}(\nu, B_{\perp})$ colormap at $D = 0.40$ V/nm. Similar oscillations are also seen in the transverse resistance with a similar period, though the effect is weaker compared to that in the longitudinal counterpart.



SI-Fig. 18: CDW phase destruction with increasing temperature: **a)** 2-d colormap of R_{xx} vs ν, T at a fixed magnetic field value of $B_{\perp} = 100$ mT for $D = 0.40$ V/nm. **b)** The periodic oscillations start diminishing with the increase of temperature with an onset temperature of $T_c^{CDW} \sim 0.6$ K which can also be seen in the Fourier spectrum colormap **c)** of **(a)**.



SI-Fig. 19: CDW at $D = 0.60$ V/nm: **a)** Similar periodic oscillations in R_{xx} vs ν can also be seen in the 2–d colormap of R_{xx} vs ν, B_{\perp} for $D = 0.60$ V/nm at $T = 25$ mK. **b)** Fourier spectrum of R_{xx} vs ν for $B_{\perp} = 120$ mT (top panel) and 2–d colormap (bottom panel) of the Fourier spectrum of **(a)**. The dominant frequency, f_{CDW} , translates to a slightly smaller oscillation period ($\Delta\nu \simeq 0.107$) compared to $D = 0.40$ V/nm. **c)** Comparison of the Fourier spectrum for $D = 0.40$ V/nm and 0.60 V/nm at $B_{\perp} = 120$ mT.

SI-14: Theoretical calculations

The electronic band structure is calculated using a tight binding model with the transfer integrals approximated under the Slater-Koster formalism using parameters from Ref. [32]. We further take care of the local curvatures at each atomic site introduced by the relaxation effects [33].

$$\begin{aligned}
\hat{\mathbf{H}} &= - \sum_{i,j} t(\mathbf{r}_{ij}) c_i^{\dagger} c_j + \text{h.c.} \\
t(\mathbf{r}_{ij}) &= t_{\pi\pi} [\hat{\mathbf{n}}_i - (\hat{\mathbf{n}}_i \cdot \hat{\mathbf{r}}_{ij}) \hat{\mathbf{r}}_{ij}] \cdot [\hat{\mathbf{n}}_j - (\hat{\mathbf{n}}_j \cdot \hat{\mathbf{r}}_{ij}) \hat{\mathbf{r}}_{ij}] + t_{\sigma\sigma} [\hat{\mathbf{n}}_i \cdot \hat{\mathbf{r}}_{ij}] \cdot [\hat{\mathbf{n}}_j \cdot \hat{\mathbf{r}}_{ij}] \\
t_{\pi\pi} &= t_{\pi}^0 \left(\frac{|\mathbf{r}_{ij}| - a_0}{\delta} \right); \quad t_{\sigma\sigma} = t_{\sigma}^0 \left(\frac{|\mathbf{r}_{ij}| - z_0}{\delta} \right) \\
t_{\pi}^0 &= -2.7\text{eV} \quad t_{\sigma}^0 = 0.48\text{eV} \quad z_0 = 3.35\text{\AA} \quad a_0 = 1.42\text{\AA} \quad \delta = 0.184\sqrt{3}a_0
\end{aligned} \tag{10}$$

In this context, \mathbf{r}_i represents the real space position of the i^{th} atom, while c_i^{\dagger} and c_i stand for the creation and annihilation operators related to the p_z Wannier orbitals at \mathbf{r}_i , respectively. The vector $\mathbf{r}_{ij} = (\mathbf{r}_i - \mathbf{r}_j)$ denotes the displacement between the positions of atoms i and j , and the unit normal at the i^{th} site is denoted by $\hat{\mathbf{n}}_i$. Additionally, $\hat{\mathbf{r}}_{ij} = \frac{\mathbf{r}_{ij}}{|\mathbf{r}_{ij}|}$ signifies the unit vector along the direction from atom j to atom i .

The effect of the electric field at each atomic site is incorporated via onsite energies

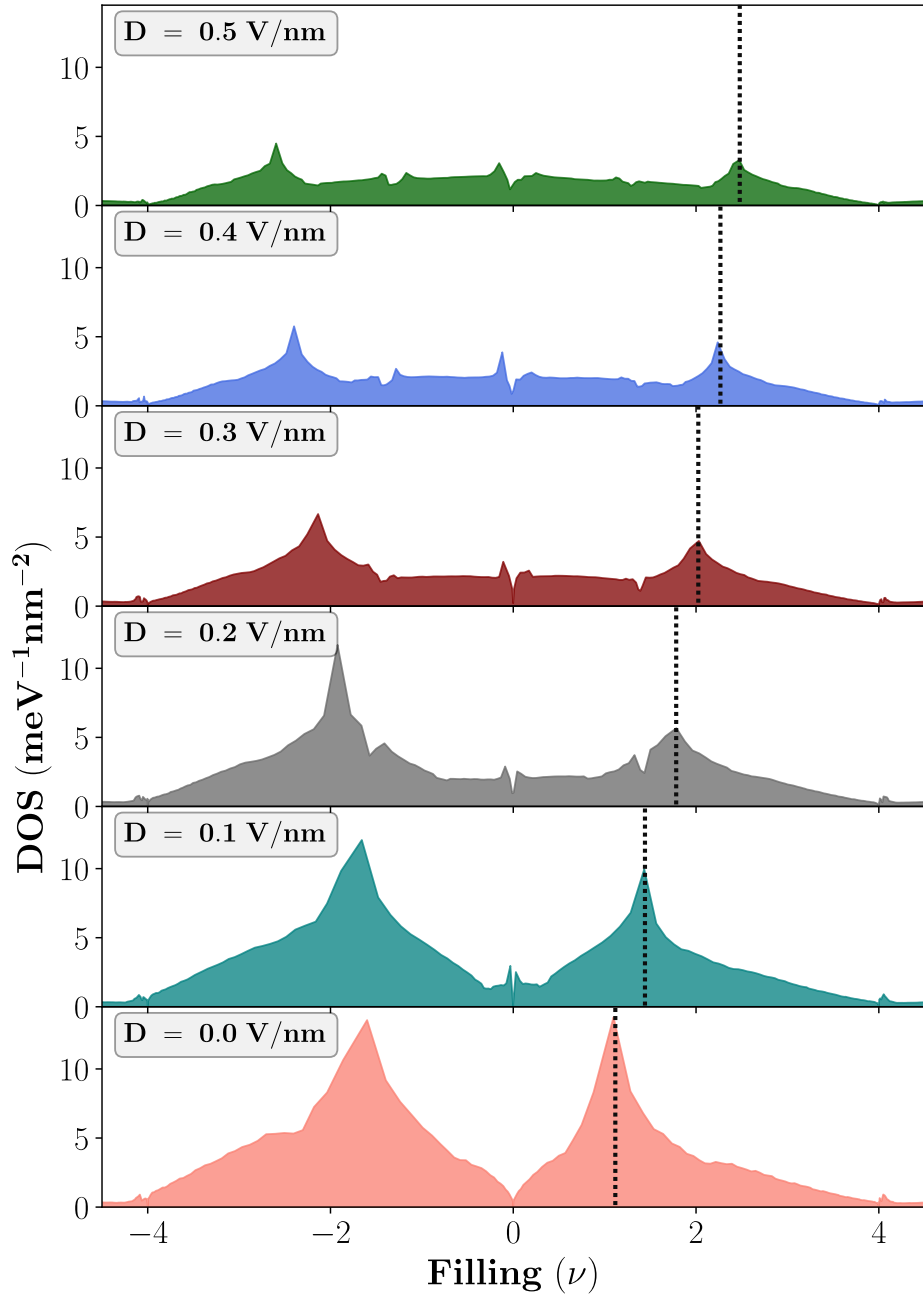
$$\epsilon_i = \begin{cases} -\frac{\Delta}{2} & \text{if } i \in \text{bottom layer} \\ \frac{\Delta}{2} & \text{if } i \in \text{top layer} \end{cases} \tag{11}$$

with $\Delta = Dz_0$, where D is the value of the perpendicular displacement field in V/nm.

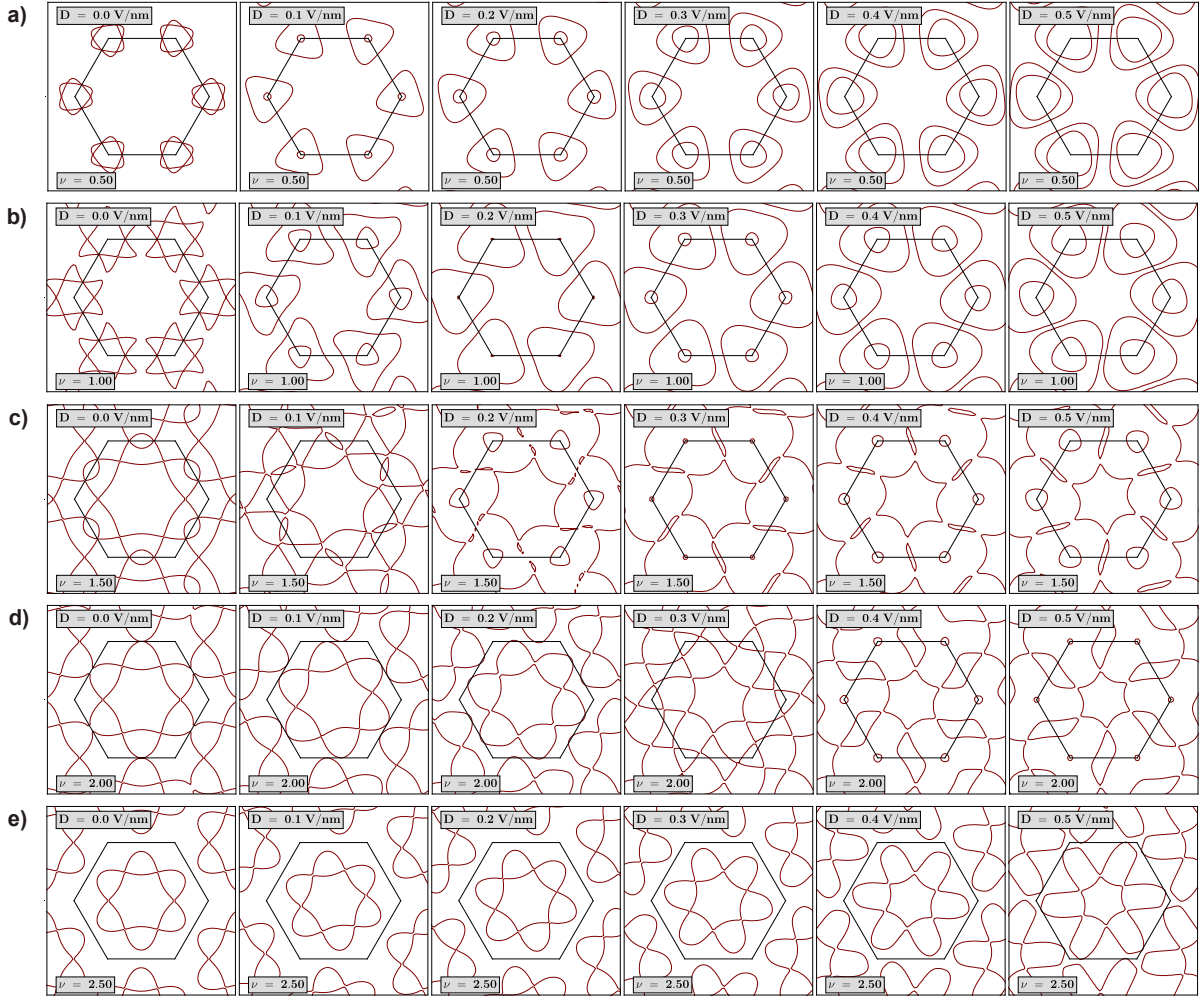
The density of states (SI-Fig. 20) and the number densities are calculated on a (40×40) \mathbf{k} grid through the linear triangulation method, which corresponds to the two-dimensional equivalent of the linear tetrahedron method. The theoretically determined van Hove Singularities (vHs) are marked as dashed lines on the

electron side. While the computed positions of the vHs deviate slightly from the experimentally observed positions, the qualitative behavior of the vHs on both the electron and hole sides, in response to the increasing displacement field, is in excellent agreement with the experimental findings.

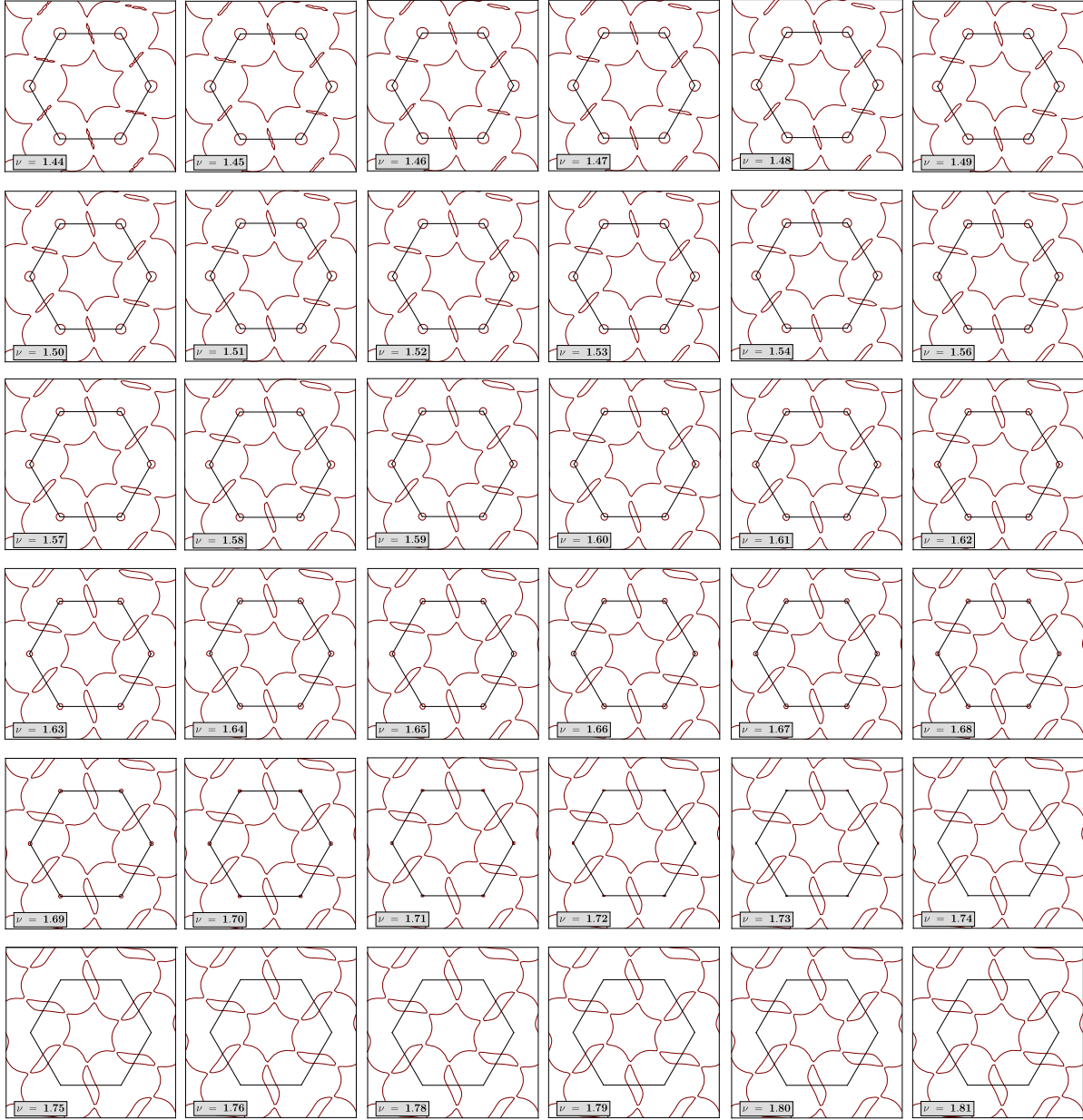
The evolution of Fermi contours within the moiré Brillouin Zone (mBZ), influenced by both displacement fields and electron doping, is illustrated in SI-Fig 21. At a displacement field of $D = 0.00$ V/nm, despite increasing levels of doping, the emergence of nested Fermi surfaces on the electron side is not observed. However, at higher displacement fields, such as $D = 0.40$ V/nm, signatures of nested Fermi contours begin to appear near the M point of the mBZ. SI-Fig 22 shows the formation and evolution of the Fermi contour nesting as a function of electron doping for $D = 0.40$ V/nm. The nested Fermi contours start forming at $\sim \nu = 1.3 - 1.4$, and the nesting vector continues to increase in magnitude till the nesting is destroyed at $\sim \nu = 2.2 - 2.3$. At a filling of $\nu = 1.60$, the nesting vector is estimated to be $\sim (1/10)^{th}$ of the reciprocal lattice vector.



SI-Fig. 20: Density of states at the Fermi energy plotted as a function of filling (ν) for different displacement fields.



SI-Fig. 21: The evolution of the Fermi contours (in all the bands that cross the Fermi level) at a fixed ν as a function of the displacement field, D , are shown in each of the rows ((a)-(e)). In the absence of a displacement field within the system, discernible indications of Fermi contour nesting are absent across all values of ν (first panel of each row). However, upon the application of sufficiently high D fields, such as $D = 0.4$ V/nm, the emergence of nested Fermi contours near the \mathbf{M} points of the Brillouin Zone becomes observable at $\nu = 1.50$. The magnitude of these nesting vectors progressively increases with ν until the nesting features disappear at very high fillings, as exemplified by the Fermi contours for $\nu = 2.5$ (bottom row panels).



SI-Fig. 22: The onset and the evolution of the nested Fermi contours at $D = 0.4$ V/nm, as a function of ν . At around $\nu = 1.60$, the magnitude of the Fermi contour nesting vector $\Delta\mathbf{q} \sim |\mathbf{k}_{\text{mBZ}}|/10$

References

1. Cao, Y. *et al.* Unconventional superconductivity in magic-angle graphene superlattices. *Nature* **556**, 43–50 (2018).
2. Cao, Y. *et al.* Correlated insulator behaviour at half-filling in magic-angle graphene superlattices. *Nature* **556**, 80–84 (2018).
3. Cao, Y., Park, J. M., Watanabe, K., Taniguchi, T. & Jarillo-Herrero, P. Pauli-limit violation and re-entrant superconductivity in moiré graphene. *Nature* **595**, 526–531 (2021).
4. Cao, Y. *et al.* Nematicity and competing orders in superconducting magic-angle graphene. *Science* **372**, 264–271 (2021).
5. Lu, X. *et al.* Superconductors, orbital magnets and correlated states in magic-angle bilayer graphene. *Nature* **574**, 653–657 (2019).
6. Yankowitz, M. *et al.* Tuning superconductivity in twisted bilayer graphene. *Science* **363**, 1059–1064 (2019).
7. Andrei, E. Y. *et al.* The marvels of moiré materials. *Nature Reviews Materials* **6**, 201–206 (2021).
8. Kim, K. *et al.* van der waals heterostructures with high accuracy rotational alignment. *Nano letters* **16**, 1989–1995 (2016).
9. Paul, A. K. *et al.* Interaction-driven giant thermopower in magic-angle twisted bilayer graphene. *Nature Physics* 1–8 (2022).
10. Ghosh, A. *et al.* Evidence of compensated semimetal with electronic correlations at charge neutrality of twisted double bilayer graphene. *Communications Physics* **6**, 360 (2023).
11. Wang, L. *et al.* One-dimensional electrical contact to a two-dimensional material. *Science* **342**, 614–617 (2013).
12. Kuir, M. *Quantum capacitance and noise measurements in van der Waals heterostructures*. Ph.D. thesis (2021).
13. Zhang, Y. *et al.* Direct observation of a widely tunable bandgap in bilayer graphene. *Nature* **459**, 820–823 (2009).
14. Su, R., Kuir, M., Watanabe, K., Taniguchi, T. & Folk, J. Superconductivity in twisted double bilayer graphene stabilized by wse₂. *Nature Materials* **22**, 1332–1337 (2023).
15. Kuir, M. *et al.* Spontaneous time-reversal symmetry breaking in twisted double bilayer graphene. *Nature Communications* **13**, 6468 (2022).
16. Sinha, S. *et al.* Berry curvature dipole senses topological transition in a moiré superlattice. *Nature Physics* **18**, 765–770 (2022).
17. Adak, P. C. *et al.* Perpendicular electric field drives chern transitions and layer polarization changes in hofstadter bands. *Nature Communications* **13**, 7781 (2022).

18. Tinkham, M. *Introduction to superconductivity* (Courier Corporation, 2004).
19. Chandrasekhar, B. A note on the maximum critical field of high-field superconductors. *Applied Physics Letters* **1**, 7–8 (1962).
20. Clogston, A. M. Upper limit for the critical field in hard superconductors. *Physical Review Letters* **9**, 266 (1962).
21. Klemm, R. A., Luther, A. & Beasley, M. Theory of the upper critical field in layered superconductors. *Physical Review B* **12**, 877 (1975).
22. Zhou, H., Xie, T., Taniguchi, T., Watanabe, K. & Young, A. F. Superconductivity in rhombohedral trilayer graphene. *Nature* **598**, 434–438 (2021).
23. Wu, S., Zhang, Z., Watanabe, K., Taniguchi, T. & Andrei, E. Y. Chern insulators, van Hove singularities and topological flat bands in magic-angle twisted bilayer graphene. *Nature Materials* **20**, 488–494 (2021).
24. Wannier, G. A result not dependent on rationality for bloch electrons in a magnetic field. *physica status solidi (b)* **88**, 757–765 (1978).
25. Lu, X. *et al.* Multiple flat bands and topological hofstadter butterfly in twisted bilayer graphene close to the second magic angle. *Proceedings of the National Academy of Sciences* **118**, e2100006118 (2021).
26. Bhowmik, S. *et al.* Broken-symmetry states at half-integer band fillings in twisted bilayer graphene. *Nature Physics* **18**, 639–643 (2022).
27. Kim, K. *et al.* Tunable moiré bands and strong correlations in small-twist-angle bilayer graphene. *Proceedings of the National Academy of Sciences* **114**, 3364–3369 (2017).
28. Tseng, C.-C. *et al.* Anomalous hall effect at half filling in twisted bilayer graphene. *Nature Physics* **18**, 1038–1042 (2022).
29. Sharpe, A. L. *et al.* Emergent ferromagnetism near three-quarters filling in twisted bilayer graphene. *Science* **365**, 605–608 (2019).
30. Lin, J.-X. *et al.* Spin-orbit–driven ferromagnetism at half moiré filling in magic-angle twisted bilayer graphene. *Science* **375**, 437–441 (2022).
31. Lin, J.-X. *et al.* Zero-field superconducting diode effect in small-twist-angle trilayer graphene. *Nature Physics* **18**, 1221–1227 (2022).
32. Moon, P. & Koshino, M. Energy spectrum and quantum Hall effect in twisted bilayer graphene. *Physical Review B* **85**, 195458 (2012).
33. Choi, S., Deslippe, J., Capaz, R. B. & Louie, S. G. An Explicit Formula for Optical Oscillator Strength of Excitons in Semiconducting Single-Walled Carbon Nanotubes: Family Behavior. *Nano Letters* **13**, 54–58 (2013).